3D printing of carbon-based materials

P. Blyweert, V. Nicolas, V. Fierro, A. Celzard

3D printing of carbon-based materials: a review

P. Blyweert, V. Nicolas*, V. Fierro, A. Celzard*

Université de Lorraine, CNRS, IJL, F-88000 Epinal, France

* Corresponding authors.

E-mail address: vincent.nicolas@univ-lorraine.fr (V. Nicolas)

E-mail address: alain.celzard@univ-lorraine.fr (A. Celzard)

Abstract

Unlike conventional subtractive methods, 3D printing allows rapid prototyping and customization on demand. However, as a process recently applied to carbon-based materials, 3D printing faces many challenges, including the precise tailoring of the printed material and the control of its porosity, as well as obtaining directly printed (pure) carbon. The present review focuses on the latest advances in carbonaceous materials in 3D printing to address these challenges. A brief introduction to additive manufacturing processes is given, followed by a summary and many recent examples of manufacturing processes, structural characteristics, and applications of various carbon-based composites and carbonaceous materials. Finally, viewpoints and prospects for this emerging field are presented.

Keywords : 3D-printing techniques, carbons-based composites, carbonaceous materials, applications

Table of contents

Nomenclature

AFM: Atomic force microscopy

AJP: Aerosol jet printing

AM: Additive manufacturing

BET: Brunauer-Emmett-Teller

BHGM: Biomimetic hierarchical graphene material

C/C: Carbon-carbon

CA: Carbon aerogel

CAD: Computer-aided design

CAL: Computed axial lithography

CB: Carbon black

CCF: Continuous carbon fiber

CCM: Carbon cellular microstructure

CF: Carbon fiber

CIJ: Continuous ink jetting

CLIP: Continuous light interface production

CNT: Carbon nanotube

CP: Cellulose powder

CV: Cyclic voltammetry

DED: Directed energy deposition

DIP: Diisodecyl phthalate

DIW: Direct ink writing

DLP: Digital light processing

DLW: Direct laser writing

DMC: Dichloromethane

DMF: Dimethylformamide

DOctP: Dioctylphtalate

DOD: Drop-on-demand ink jetting

DVB: Divinylbenzene

EIS: Electrochemical impedance spectroscopy

ESEM: Environmental scanning electron microscopy

FDM: Fused deposition modeling

FFF: Fused filament fabrication

GA: Graphene aerogel

GF: Gage factor or Graphene foam (depending on the context)

GO: Graphene oxide

hGO: Holey graphene oxide

HTT: Heat-treatment temperature

IDE: Interdigitated electrode

IFN-γ: Interferon-gamma

IL-10: Interleukin-10

IPA: Isopropyl alcohol

LOM: (Laser-assisted) Laminated object manufacturing

LS: Lignosulfonate

MFC: Microbial fuel cell or Micro fibrillated cellulose (depending on the context)

MSC: Microsupercapacitor

MWCNT: Multiwalled carbon nanotube

NEP: Noise-equivalent power

PCP: Porous carbon platelet

PDMS: Polydimethylsiloxane

PEEK: Polyether ether ketone

PET: Polyethylene teraphtalate

PETA: pentaerythritol tetraacrylate

PI: Polyimide

PLA: Polylactic acid

PR-IDE: Photoresin interdigitated electrode

PVA: Polyvinyl alcohol

RFA: Resorcinol/formaldehyde aerogel

rGO: Reduced graphene oxide

SEM: Scanning electron microscopy

SLA: Stereo-photolithography – Stereolithography

SLM: Selective laser melting

SLS: Selective laser sintering

SWCNT: Single-walled carbon nanotube

TEM: Transmission electron microscopy

TENG: Triboelectric nanogenerator

TPP/2PP: Two-photon polymerization

UAM: Ultrasonic additive manufacturing

1. Introduction

Additive manufacturing (AM), known as rapid prototyping, rapid manufacturing, or more commonly 3D printing, is the "process of joining materials to make parts from 3D model data, usually layer upon layer" [1]. In contrast to conventional methods such as subtractive manufacturing, AM allows the production of a finished product on demand from computer-aided design (CAD) models **(Figure 1)**.

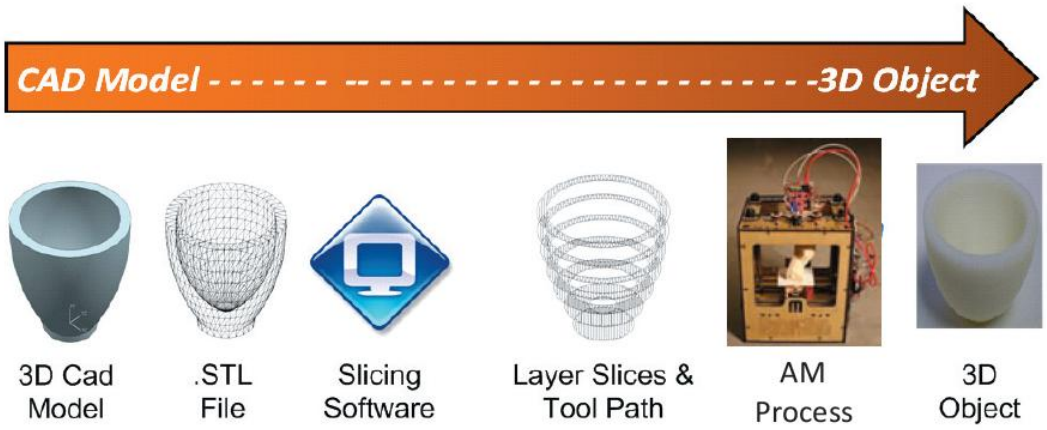

Figure 1. Generalized 3D-printing process [2]. Copyright 2011, Atlantic Council.

This technology has emerged and evolved, since the 1980s [3–5], as a versatile technology for fabricating complex structures from various materials [6,7] such as biomaterials [8], polymers [9–12], ceramics [13], glass [14,15], metals [16], polymerized ionic liquids or even food [17,18]. It has opened up new opportunities for many different applications, including building [19], aerospace [20], catalysis [21], medical [22–25], among many others. Due to the diversity of printing methods and materials, 3D printing is a powerful technology for advanced manufacturing, both for academic research and industrial production.

Carbonaceous materials, thanks to their excellent chemical stability, their versatile nanostructure, and their special mechanical, electrochemical, thermal, and electrical properties, have been extensively used in 3D printing. Indeed, in recent years, with the development of 3D-printing technologies, the applications of carbon have undergone

unprecedented changes. Researchers have begun to use AM to manufacture very complex systems that could never be achieved (or with great difficulty) by conventional methods, particularly in energy applications [26–28]. To date, much effort has been devoted to the development of a wide variety of carbonaceous materials printed in 3D with different morphologies using carbon fibers [29], carbon black, carbon nanotubes [30], graphene, and graphene oxide [31], which are easily printable using a binder matrix. In contrast, less attention has been paid to glassy and porous carbons that are obtained from printed carbon precursors.

As additive manufacturing is not directly applicable to pure carbon, since this particular element can neither be melted, sintered nor polymerized, the printing of pure carbon materials is still in its early stages of development. Existing studies have reported several challenges, including adjusting the properties of the printed materials and their porosity [32–34], increasing the carbon content of printing or printed materials [35], and difficulties in directly achieving a high-carbon content structure [36,37]. As carbon can be considered alone or in the presence of a binder, which is completely different as shown below, it is then necessary to take into account the great diversity of carbonaceous materials in order to better reflect the strong potential of their 3D printing, but also to take into account the diversity of 3D-printing processes.

The aim of this review is then to discuss the most recent advances in 3D carbon printing, typically over the past 5 years, and to provide comprehensive insights into the printing of functional carbon-based systems. In this perspective, we will highlight 3D printing of carbon-filled composites and carbon precursors, discussing at the same time several emerging applications. Finally, we share our perspective on future directions.

2. Overview of 3D-printing technologies

During printing, patterned areas composed of building material (referred to as resins, powders, filaments, or inks depending on the technology) are solidified (or crosslinked) into a structure with a certain function, usually a given mechanical property. In order to meet this requirement, the various material printing techniques have been classified by ASTM into seven categories: powder bed fusion, material extrusion, material jetting, binder jetting, vat photopolymerization, sheet lamination, and directed energy deposition [1].

Selective laser sintering, vat photopolymerization, and directed energy deposition selectively solidify the print material from a material tank (or material feeder) according to the sliced pattern. In contrast, inkjet printing, binder jetting and material extrusion deliver the print material through a print head or nozzle to a designated position prior to curing. Whereas in the sheet lamination process, the print material is physically bonded without curing.

A comprehensive comparison of these 3D printing technologies is shown in **Table 1** and the corresponding processes are thoroughly detailed in the Supplementary Information. Each method has its advantages and drawbacks in terms of resolution, applicable materials or printing speed, but their performance depends on the printing requirements.

Table 1. Comparison of different 3D-printing techniques.

Printing technique	Process	Typical Materials	Strengths	Weaknesses	Resolution (µm) and reference
Powder Bed fusion	Selective Laser Sintering (SLS)	Plastics, Metal and Ceramic Powders, Sand	High level of complexity No support material required Wide range of materials	Poor surface quality Require post-processing treatments	> 50 [38]
	Selective Laser Melting (SLM)				
Material Extrusion	Fused Deposition Modelling (FDM); Fused Filament Fabrication (FFF)	Thermoplastic Filaments and Pellets, Slurries	Inexpensive, good structural properties	Layer-by-layer appearance Poor surface quality High delamination risk	50-200 [39]
	Direct Ink Writing (DIW)	Slurries, Gels		Fixed resolution	1-100 [40]
Material Jetting	Ink Jetting	Photopolymers, Polymers, Waxes	High level of accuracy and complexity Enable multiple materials in a single part	Expensive materials and printer Need of support material	5-200 [41]
	Aerosol Jetting			Lack of parallel deposition Long processing time	≈ 10 [42]
Binder Jetting		Powdered plastics, Metals, Ceramics, Glass, Sand	High productivity, wide range of materials	Poor mechanical properties Low definition	> 50 [43]
Vat Photo-polymerization	Stereolithography (SLA)	Photopolymers: acrylates, epoxies, filled resins (glass, ceramic, metal, …), …	High level of accuracy and complexity, Smooth surface finish	Significant cost of photopolymers Relatively slow printing process Require post-processing treatments	> 10 [44,45]
	Digital Light Processing (DLP)				> 5 [46]
	Continuous Light Interface Production (CLIP)				> 5 [47]
	Two-Photon Polymerization (TPP); Multiphoton polymerization (MPP); Direct Laser Writing (DLW)				> 0.1 [48,49]
	Computed Axial Lithography (CAL)				≈ 300 [50]
Sheet Lamination	Laminated Object Manufacture (LOM)	Paper, Plastic Sheets, Metal foils	High volumetric build rates	Misalignment of layers Bonding efficiency impacted by laser cut	Depends on the thickness of the laminates
	Ultrasonic Additive Manufacturing (UAM)		Allows the combinations of metal foils, including embedding components	Limited to metal foils Not adapted to finely detailed structures	
Directed Energy Deposition (DED)		Metal Wire and Powder with Ceramics	High single-point deposition rates	Low resolution Reduced ability to manufacture complex parts	> 250 [51]

3. 3D printing of carbon-filled composites

Composites generally combine a matrix and fillers to achieve structural or functional properties that cannot be achieved by the constituents alone. Carbons are often used as functional fillers, either to improve the mechanical properties of the matrix material or to give it new properties (thermal, electrical, biocompatibility, etc.). Carbon-filled composites are a class of materials whose properties vary according to their composition (type of filler, filler architecture and orientation, matrix density, amount and type of defects, etc.) and their method of preparation. Strength and fracture toughness, mainly determined by the intrinsic properties of the phases present and the strength of the bond between filler and matrix, or electrical conductivity, governed by the contacts between fillers, are often discussed in the literature [52].

3.1 Mechanical reinforcement of polymers

Pure polymers have limited mechanical properties, which reduces their potential applications. Combining multiple materials or a matrix filled with particles to achieve the desired mechanical properties is a common method. Many research teams have developed new printable materials reinforced with carbon fibers or nanoparticles, such as multi-walled or single-walled carbon nanotubes (MWCNTs or SWCNTs).

3.1.1 Carbon fiber composites

Jansson and Pejryd studied the behavior of commercial polyamide (PA12)/carbon fiber (CF) composites printed by SLS process [53]. Details on the SLS technique are available in the Supplementary Information. With the addition of short carbon fibers (100-200 µm in length), the mechanical properties of tensile bars manufactured along several directions in the build chamber (*x*, *y*, *xy*, *x* 45°, *y* 45° and *xy* 45°, see **Figure 2a**) and measured by a tensile test were significantly improved. Indeed, compared to a virgin polyamide rod, the tensile strength

increased by 28 % and 12 % for the *x* and *y* directions, respectively **(Figure 2b)**. The homogeneous porosity in the interlayer planes of the structure (around 12 %) and the poor fusion of the layers in the bar build in the *y*-direction explained the limited increase of the tensile strength. The authors noticed that this interlayer porosity, resulting from a difficult packing of the CF/PA12 powder and increasing with the number of laser sweeps, significantly weakened the material in the *z*-direction of the build chamber, as tilted bars fractured at the interlayer bonding area. Moreover, the reduced mechanical properties in the build plane were mostly due to the fiber orientation. The rake spreading the powder before each layer moves in the *x*-direction and aligns the fibers preferentially in that direction., with very few fibers penetrating in between layers in the *z*-direction, hence the observed reinforcement effect.

Thus, this raised a research topic on the processability and granulometry of powders for carbon-containing composites, which could lead to a limitation of the material properties.

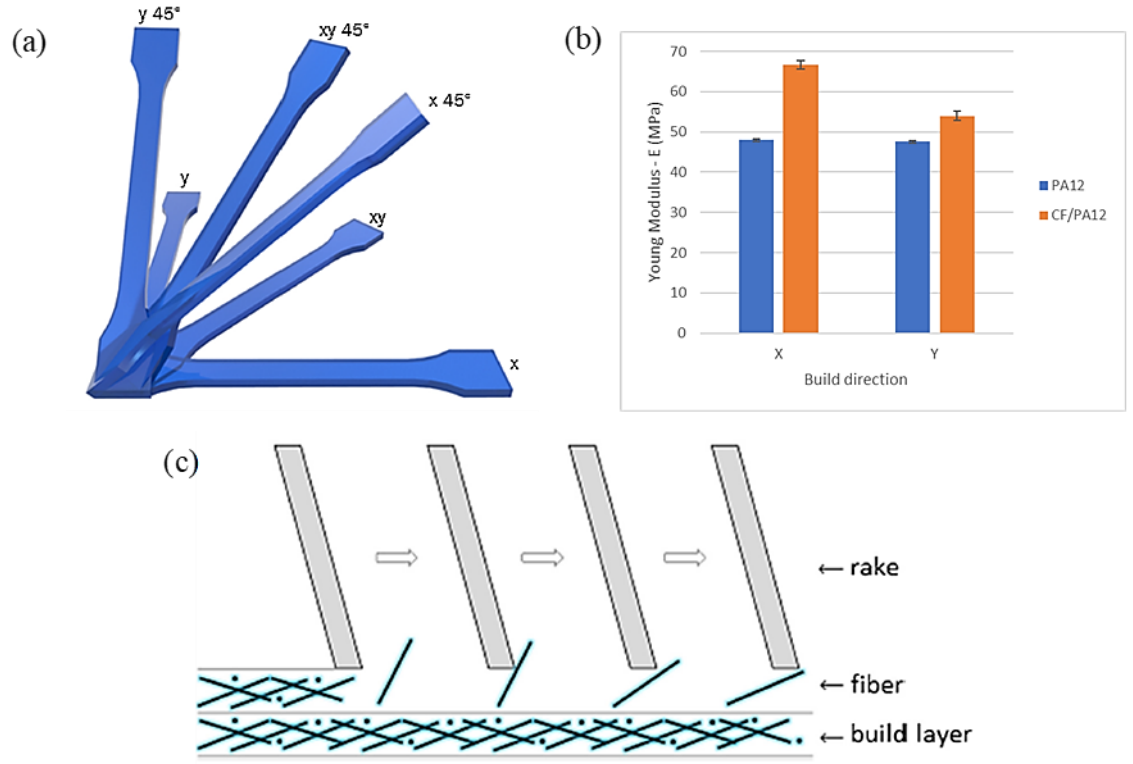

Figure 2. (a) Manufacturing orientation of the tensile bars in the build chamber. The powder spreading rake moves in the *x*-direction; (b) Tensile test results for PA12 and CF/PA12 specimens built in the *x* and *y* directions; (c) Illustration of the rake spreading a powder layer in the SLS build chamber. Fibers that are not oriented in the plane of the build chamber will be aligned by the action of the moving rake. Reproduced and redraw with permission from [53]. Copyright 2015, Elsevier.

It is well understood that by adding CF in dry powder form, the spreading mechanism allows the fibers to be oriented in the *x* and *y* direction and thus improve the corresponding mechanical properties **(Figure 2c)**, but the performance improvements, especially in the *z*-direction, are not as great as expected. Considering the importance of particle size and powder flow behavior for the SLS process, Chen et al. [54] suggested that a milling process followed by sieving could successfully lead to a powder based on composite grains of short carbon fibers encapsulated in Polyether Ether Ketone (PEEK) (in **Figure 3**, the resulting fractions of

CF at 33, 34 and 54 wt.% are called A, B and C, respectively). As expected by the authors, a standard CF-reinforced, hot-compression molded sample showed higher modulus compared to the laser-sintered film (7297.4 and 2749.1 MPa, respectively for fraction B, measured at 100 °C). Nevertheless, the laser-sintered sieved composite sample showed an increase in complex modulus (E^*) compared to the dry blend samples (2749.1 MPa vs. 936.5 MPa at 100 °C) and even more after double laser sintering (increase of about 140 % at 100 °C). This confirmed the efficiency of the sieving method for the preparation of CF composite powder for SLS but at the same time highlighted the limited added value of SLS in terms of mechanical properties compared to molding techniques.

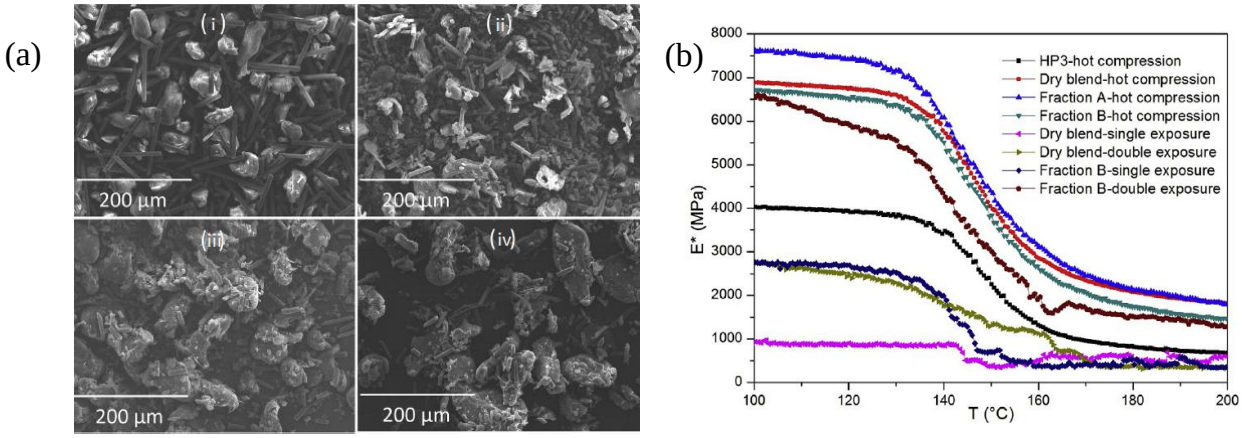

Figure 3. (a) SEM images of powders: (i) dry blend [33 wt.% CF], (ii) fraction A [54 wt.% CF], (iii) fraction B [34 wt.% CF], (iv) fraction C [33 wt.% CF]; (b) Complex modulus (E^*) of hot-compressed and laser-sintered samples measured by DMTA. Reproduced with permission from [54]. Copyright 2019, Elsevier.

A significant increase in mechanical properties has also been reported for FDM printing of carbon fiber-reinforced thermoplastic matrix. Details on the FDM technique are available in the Supplementary Information. Tian et al. [55] considered the different printing parameters (extrusion temperature, layer thickness, hatching, etc.) in order to find the best conditions for printing CCF-PLA composites with improved mechanical properties. Temperature

optimization in the range 200-230 °C increased the melt flow capability of PLA and helped to improve the impregnation of the carbon fibers by PLA. This led to a high flexural strength of 335 MPa with a layer thickness of 0.5 mm, hatching of 0.4 mm and a fiber content of 27 wt.%.

Recently, Heidari-Rarani et al. [56] studied the mechanical properties of PLA reinforced with continuous carbon fibers (CCF, 1000 filaments per fiber). Compared to pure PLA, the ultimate tensile strength of the composite increased by about 36 % **(Figure 4)**. This preparation based on the "Embedding on the component" method proved to be effective because the dominant failure modes were delamination and delamination-induced matrix cracking, and not fiber/matrix de-bonding.

(a)

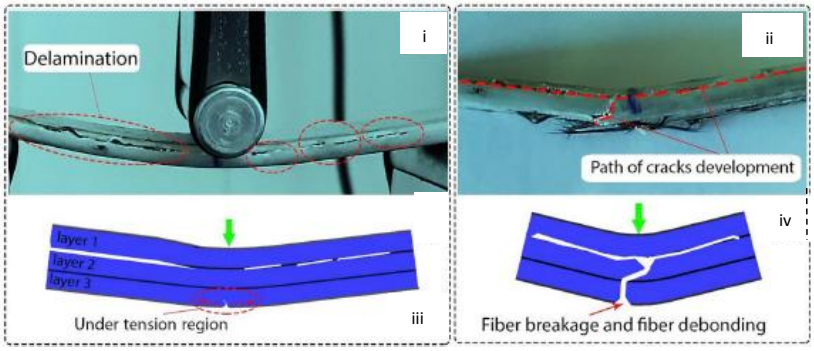

(b)

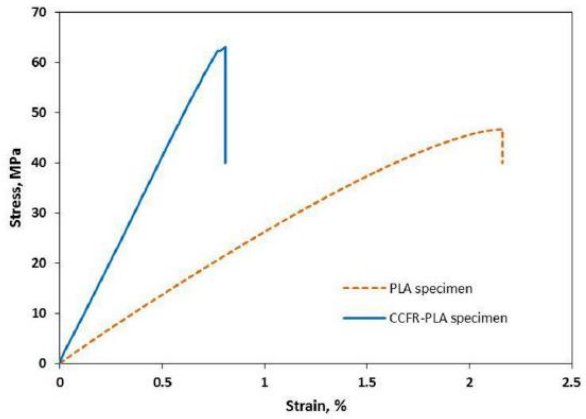

Figure 4. (a) Failure modes of a specimen of CCF-PLA in a bending test: (i) specimen under bending test and initiation of delamination, (ii) specimen after failure and fiber breakage, (iii) schematic view of the bending test, (iv) scheme of the final failure; (b) Tensile stress-strain

curves of pure PLA and CCF-PLA specimens. Reproduced with permission from [56]. Copyright 2019, Elsevier.

The reported results were even better with a 77 % increase in tensile yield stress for polycarbonate reinforced with three bundles of carbon fibers with 12000 filaments per bundle [57], and even higher for carbon fiber-reinforced thermoplastic polyimide (TPI) with separated 3D-printing of CCF (1000 filaments per fiber) **(Figure 5a)** [58]. Indeed, the reported values of tensile strength were respectively 214 % and 158 % higher than the pure TPI and the usual continuous carbon fiber printing (named in this study "Original continuous carbon fiber" method, see **Figure 5b** and **Figure 5c**). Surprisingly, due to a loose combination of materials and the presence of air inclusions, the addition of short CF at about 5 wt.% by mixing pure TPI with commercial CF/TPI composite led to a decrease in performance of about 25 % when compared to pure TPI.

However, thanks to a better impregnation of the fibers, a synergistic reinforcement effect on the mechanical properties of 3D-printed composites with short and separated continuous carbon fibers can be observed [59]. This synergistic effect can be further tailored with the raster angle of the continuous fibers, different stacking sequences (concentrated or separated distribution of CCF) and different loading directions (parallel or perpendicular to the thickness direction), allowing for the production of rigid or high energy absorbing structures [60].

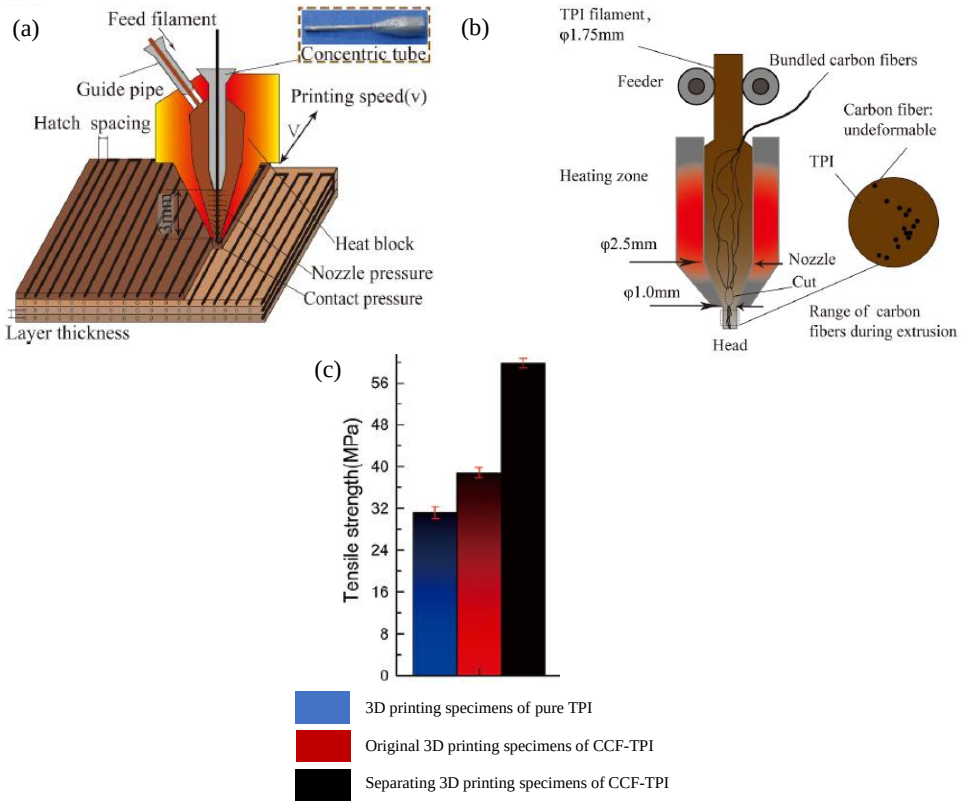

Figure 5. (a) Scheme of 3D printing of separated continuous carbon fiber-reinforced TPI: the carbon fiber is driven to the nozzle using a concentric tube, which reduces the contact length and contact time between the TPI and the carbon fiber; (b) Original continuous carbon fiber printing scheme: the carbon fiber is directly fed into the heat sink and extruded with the TPI filament. This method often results in an interruption of the carbon fiber supply, which has a significant impact on the mechanical propertie of the samples; (c) Tensile strengths of pure TPI, original and separated 3D-printed continuous CF/TPI. Reproduced in parts with permission from [58]. Copyright 2019, Elsevier.

As a novel approach to continuous carbon fiber (CCF)-reinforced thermoplastic printed in 3D, Parandoush et al. [61] studied a laser-assisted LOM technique (LA-LOM). Details on this technique are available in the Supplementary Information. Laminates were prepared with unidirectional polyamide-6 (PA6) prepregs with continuous carbon fiber (CCF, 48.5 wt.%) and then bonded with a CO_2 laser and consolidated with a roller system. The authors claimed

that the mechanical properties of CCF/PA6 composites printed with this new method are superior (flexural and tensile strengths of 668.3 MPa and 591.5 MPa, respectively) to those of carbon fiber-reinforced composites printed with FDM, SLA or SLS **(Figure 6)**.

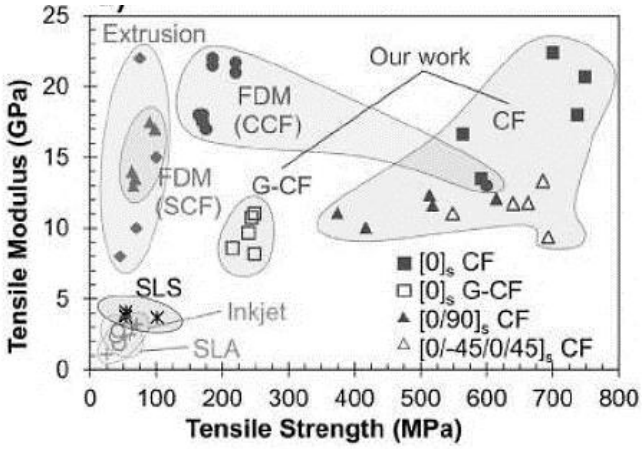

Figure 6. Space map of tensile modulus versus tensile strength comparing LOM-printed CCF-PA6 with other CF-reinforced polymers printed in 3D with other methods, namely FDM, DIW, SLS, inkjet, and SLA. Reproduced with permission from [61]. Copyright 2019, Wiley-VCH.

Chang et al. [62] have also reported the mechanical improvement of carbon fiber-reinforced PEEK laminates containing 59 vol.% continuous carbon fibers prepared by the LA-LOM technique **(Figure 7a)**. Bending and tensile tests with different orientations were carried out on samples before and after hot press post-processing (HPP, 370 °C, 150 kPa, 80 min). The flexural and tensile strengths of samples after HPP were higher than those of non-treated samples with an increase in properties of 183.5 % and 24.8 %, respectively, for samples with fibers aligned along the prepreg *x*-direction **(Figure 7b)**. The flexural and tensile strengths of the two CCF/PEEK samples produced in this work were also higher than those of the FFF-printed carbon fiber-reinforced thermoplastic.

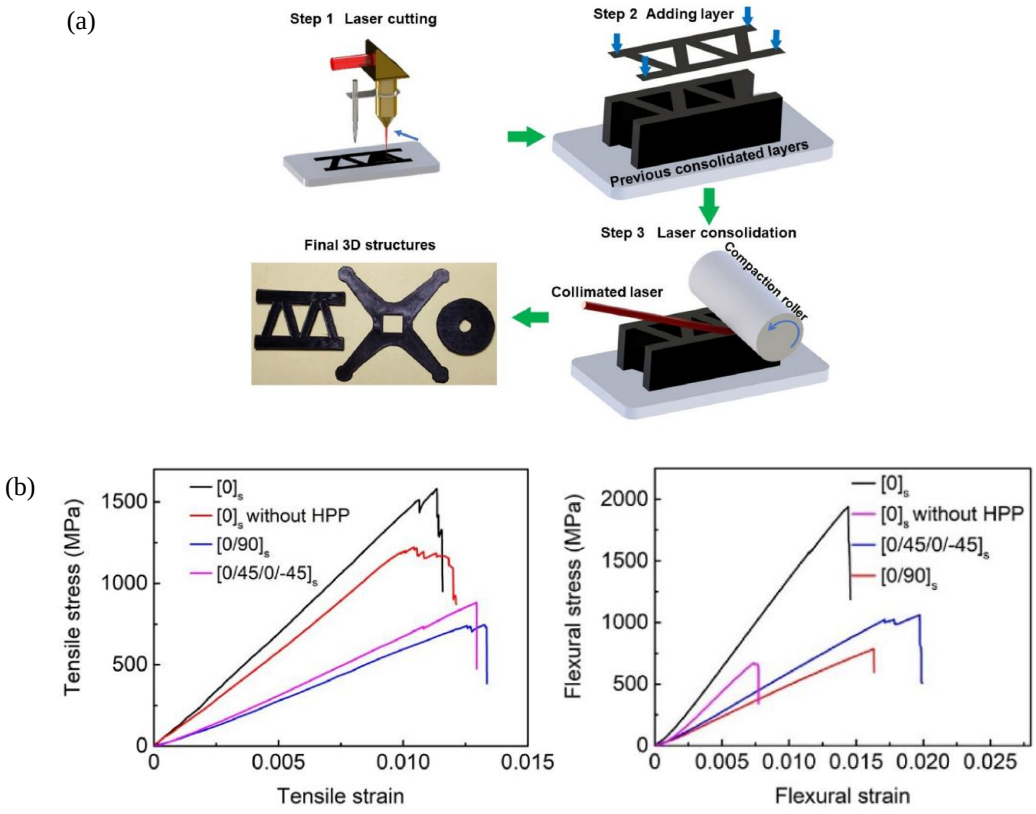

Figure 7. (a) Scheme of the LA-LOM 3D-printing process of CCF/PEEK parts; (b) Tensile (left) and flexural (right) stress-strain curves. Reproduced with permission from [62]. Copyright 2020, Elsevier.

Recently, ultrasonic additive manufacturing (UAM) was investigated by Guo et al. [63] as a new method of manufacturing continuous carbon fiber-reinforced polymer composites with aluminum alloy **(Figure 8a)**. Details on the UAM technique are available in the Supplementary Information. The carbon fiber tow was woven to produce loops along the sides and was coated with epoxy resin, which was cured at room temperature. Thin aluminum sheets were then welded under and over the carbon fiber composite to form laminates with a continuous joint. Samples with 3 and 4 CF-embedded layers were produced and analyzed. The peak tensile load was almost doubled by increasing the number of layers by 1 (from 4677 N to 7238 N for 3 and 4 layers, respectively, see **Figure 8b**). The authors also noted that the

failure modes could easily be modulated by the number of layers of CF-epoxy composite, the number of CF tows, or the CF/aluminum ratio.

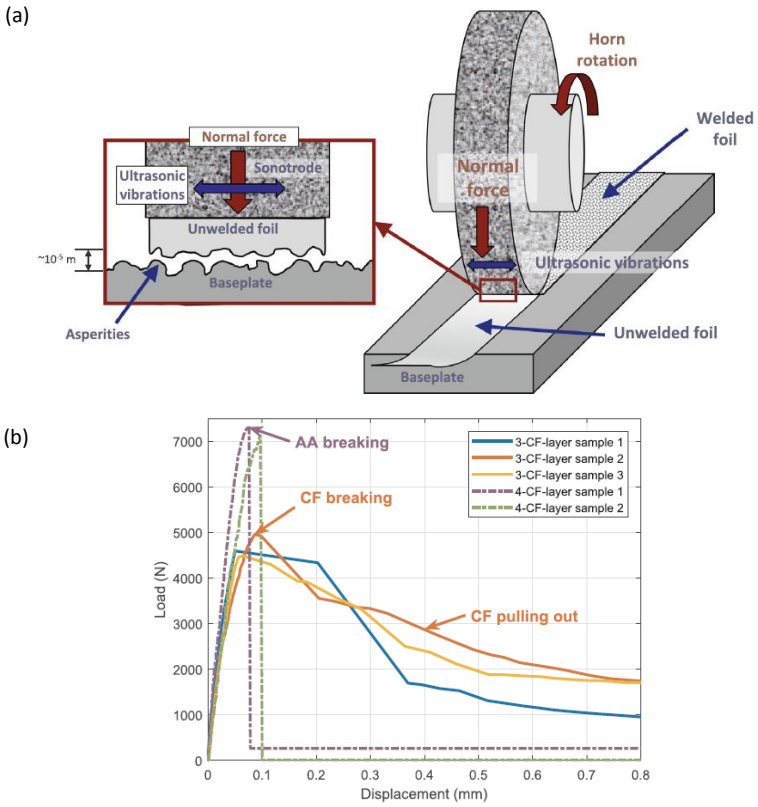

Figure 8. (a) Ultrasonic additive manufacturing process (not to scale); (b) Load-displacement curves for the tensile test of samples with 3 and 4 layers of CF-based composites. Reproduced with permission from [63]. Copyright 2018, Elsevier.

All these studies have provided an efficient method for building carbon fiber-reinforced polymer structures. Nevertheless, polymer-based composites are not always applicable to severe environmental conditions, especially at high temperatures. Thus, Yi et al. [64] developed a multi-step procedure **(Figure 9)** combining SLS printing and chemical vapor infiltration (CVI) to prepare carbon/carbon (C/C) composites. A phenolic resin/carbon fiber powder was prepared with 40-60 wt.% of short CF and processed. The C/C green body was treated by CVI and then carbonized **(Figure 9a)**. The authors noted that the flexural strength of specimens increased with CF content and density (by 235.9 % and 238.1 % for 60 wt.% CF

specimens at densities of 1.3 and 1.5 g cm^{-3}, respectively, see **Figure 9b**). This 3D-printing method can be well applied to the production of C/C composite parts with high mechanical performances that could meet requirements that carbon fiber/polymer composites cannot achieve.

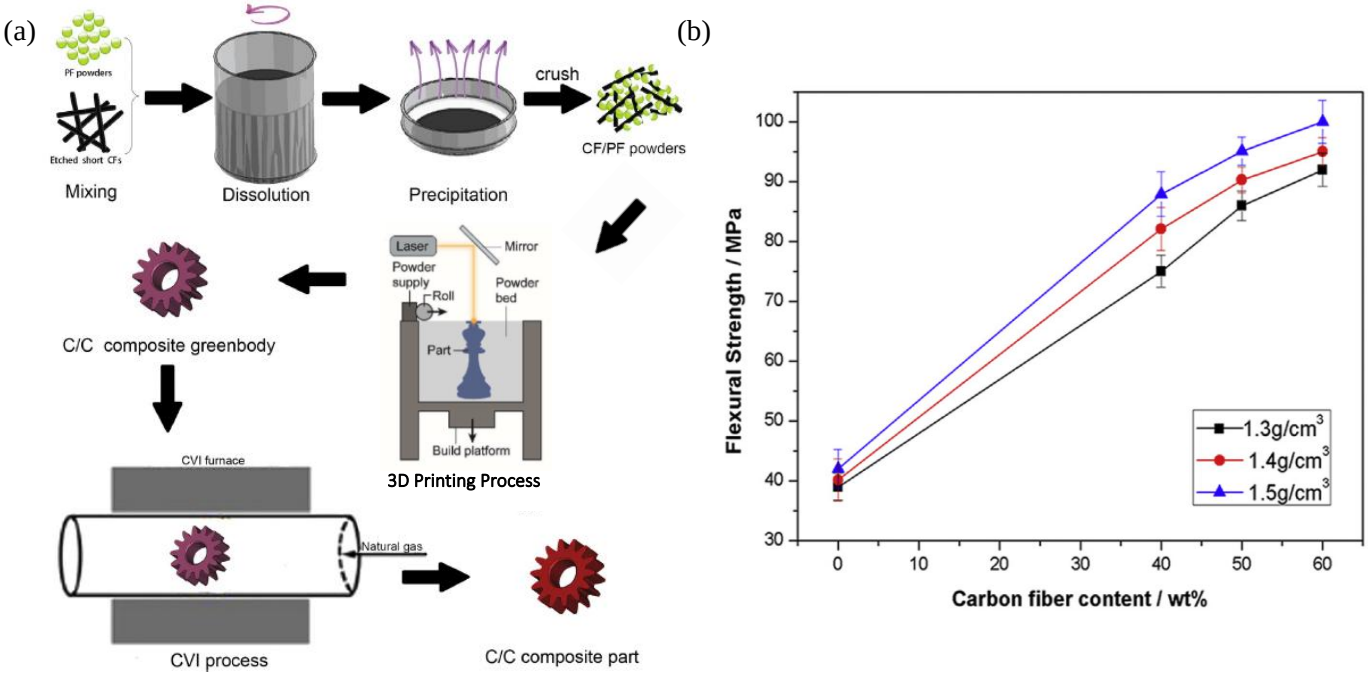

Figure 9. (a) Overview of the preparation of a complex carbon/carbon composite part; (b) Variation of the flexural strength of the corresponding C/C composite parts printed in 3D with different carbon fiber content and densities. Adapted with permission from [64]. Copyright 2015, Elsevier.

3.1.2 Carbon nanotube composites

In addition to carbon fibers, the use of carbon nanoparticles, especially CNTs as reinforcing filler in a metal matrix, is also known. Wang et al. [65] presented a MWCNT/Inconel 625 composite. The composite powder prepared by sonication of 0.5 wt.% of surface-modified MWCNTs with Inconel 625 was then processed by the SLM technique **(Figure 10a**, details available in the Supplementary Information**)**, and finally some samples were heat-treated at 1040 °C for 2 h followed by aging at 720 °C for 7 h and at 650 °C for 8 h.

As expected, the tensile strength increased by 14 % compared to the Inconel standard for both heat-treated and untreated samples **(Figure 10b)**. Due to the increase in grain size, the elongation at break of the heat-treated samples was increased by 50 % compared to the untreated samples and was close to that of the Inconel standard. Furthermore, microstructural analyses suggested that even at low content, MWCNTs increased the thermal conductivity of the metal matrix (the cooling rate increased from 1.4×10^5 K s^{-1} to 1.8×10^5 K s^{-1}).

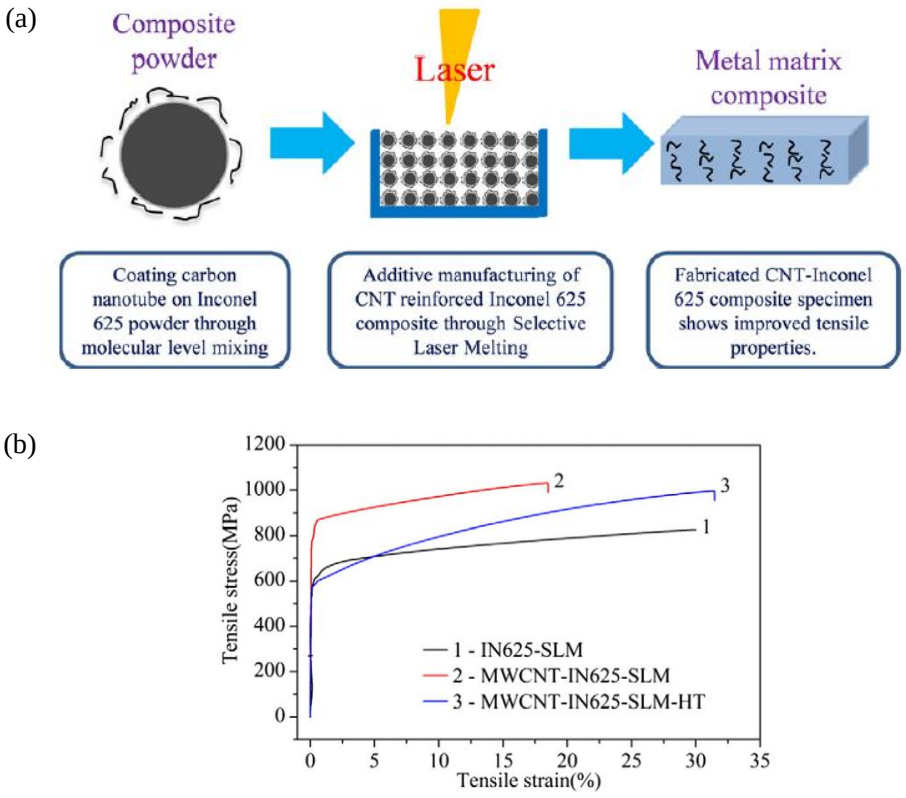

Figure 10. (a) Schematic manufacturing process of thermally conductive CNT-Inconel 625 composites; (b) Corresponding strain-stress curves. Reproduced with permission from [65]. Copyright 2016, Elsevier.

Recently, Kutlu et al. [66] presented a directed energy deposition (DED) approach to form PA/CNTs composites **(Figure 11a)**. Details on the DED technique are available in the Supplementary Information. DED was adapted for use with thermoplastics using a Yb-doped fiber laser (wavelength 1075 nm) and a powder feed from a coaxial powder nozzle. PA

powder was mixed with 1.25 wt.% of additives in the form of a mixture of equal amounts of nanosized silica (flow additive) and MWCNTs (optical absorber, antistatic aid, and mechanical filler). Specimens for tensile tests were produced, both in the direction perpendicular and parallel to the build platform. The samples printed with their principal axis in the *x*-direction, thus parallel to the successive deposited layers, showed a higher ultimate tensile stress than the samples generated perpendicular to the layers **(Figure 11b)**, with values of 5.1 MPa and 4.2 MPa, respectively, demonstrating the effect of low MWCNT content in the matrix. Nevertheless, these results were much lower than those prepared by SLS with PA/carbon black (4 wt.%) powder and even lower than those obtained for injection-molded specimens. This poor performance is probably due to the high porosity of the DED-printed sample but also to poor particle/matrix interaction. These results highlighted the limitations of powder printing and the need for a careful approach to the design of CNT-based composites, as discussed by Kinloch et al. [67].

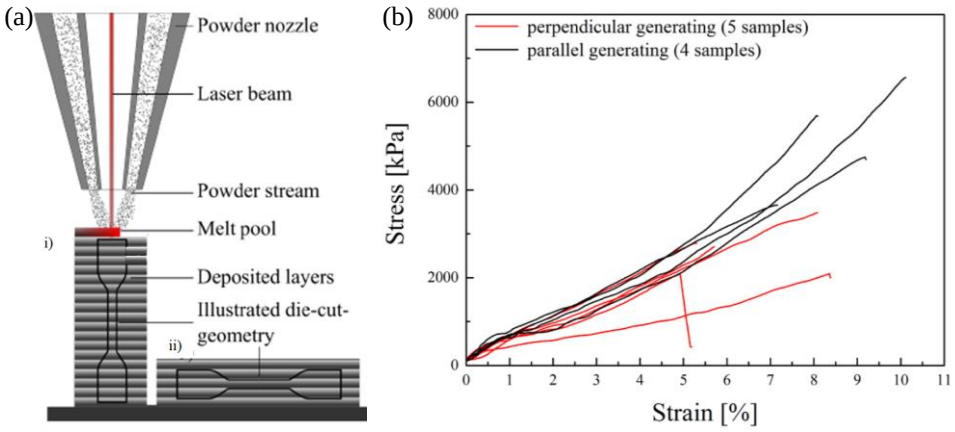

Figure 11. (a) Schematic DED process and the two building strategies to generate specimens for mechanical tensile testing, after die-cutting: (i) specimen with layers perpendicular to the tensile axis, and (ii) specimen with layers parallel to the axis; (b) Corresponding strain-stress curves. Reproduced under terms of the CC BY-NC-ND license from [66]. Copyright 2020, Elsevier.

The difficulties to ensure a homogeneous dispersion of MWCNTs in thermoplastics, thus leading to poor filler/matrix interaction, is the main issue affecting the properties of composites. Sezer et al. [68] illustrated this particular challenge with an ABS matrix reinforced with high MWCNT loading and printed by FDM. The ultimate tensile strength of the specimens increased to its maximum at 7 wt.% loading (288 % increase compared to raw ABS), but decreased at higher loading due to agglomeration of the nanoparticles.

These various attempts have shown an improvement in the mechanical properties of 3D-printed matrices (thermoplastic and metal) with the additions of carbon fillers, revealing their potential in demanding applications in terms of strength. However, for some applications with simple structures, 3D printing does not provide any real added value compared to molding, especially in terms of mechanical properties.

For some applications, the material must have functionalities such as electrical conductivity or microwave absorbing properties. As most matrices, especially pure polymers, do not have these properties, the addition of a functional filler is often the best option. Electrical conductivity is essential for flexible and wearable electronics. Conductive additives such as carbon black (CB), carbon nanotubes (CNT), and graphene are commonly used to modify matrix properties. **Table 2** summarizes the effects of different reinforcements and 3D-printing technologies on thermoplastic/carbon composites.

Table 2. Summary of the effect of carbon reinforcement on 3D printing of composites

Technique	Composite	Improvement over unfilled matrix 3D-printed in the same way	Remarks	References
SLS/SLM	PA12 / Short CFs	Improvement of tensile strength up to 28 % in *x*-direction	Preferred orientation of fibers and preferred printing direction led to improved mechanical properties compared to printed matrix, which, however, remained lower than those of molded sample due to high interlayer porosity.	[53]
	PEEK / Short CFs	Modulus improvement of 293.5 % at 30 wt.% filling		[54]
	Phenolic resin / Short CFs	The flexural strength increased by more than 235 %	Combination of SLS and CVI at high CF loading. The flexural strength increased with parts density.	[64]
	Inconel 625 / MWCNTs	The tensile strength and elongation at break increased by 14 % and 50 %, respectively	The good CNT dispersion also improved the thermal conductivity of the metal matrix	[65]
FDM	PLA / CCF (1000)	The tensile strength increased to 335 MPa with a fiber content of 27 wt.%	Effects of printing parameters on mechanical properties were observed at high fiber contents	[55]
		The tensile strength increased by 36 % and the flexural strength increased to 345 MPa	No fiber/matrix debonding due to a good impregnation	[56]
	Polycarbonate / CCF (12000)	The tensile yield stress increased by 77 %	The tensile yield strength varied with the number of embedded bundles	[57]
	TPI / Separated CCF (1000)	The tensile strength increased by 214 % compared to pure TPI and by 158 % compared to usual CCF/FDM	Possible air inclusions leading to decrease of performance when adding short CFs	[58]
	PA / Separated CCF/ Short CF	Increase of tensile strength above 400 MPa for 6 CCF-laminated composites	A synergistic reinforcement effect (depending on printing parameters) with good fiber impregnation was observed.	[59,60]
LOM	PA6 / CCF	Improvement of flexural and tensile strength	The obtained mechanical properties were superior to those of other CF-reinforced composites printed with other techniques.	[61]
	PEEK	Flexural strength increased by 183.5 % and tensile strength by 24.8 %	Need of thermal post-processing to obtain such properties.	[69]
UAM	Epoxy / CF / Aluminum	The tensile load doubled when increasing the number of embedded layers from 3 to 4	Modulation of mechanical reinforcement with the number of layers, tows and Al ratio but the technique is yet limited to Al or thin metal foils.	[63]
DED	PA / CNTs	Increase of ultimate tensile stress to 5.1 MPa	The increase of porosity negatively impacts the properties of the parts.	[66]

3.2 Electrical conductivity

Hong et al. [70] made carbon black (CB) nanoparticles absorbed by polyamide (PA) powder to obtain a conductive matrix printable by SLS **(Figure 12a)**. When the CB content increased from 0 to 2 wt.%, the electrical conductivity of the SLS-printed specimen jumped from 2.86×10^{-10} to 2.05×10^{-4} S m^{-1}, while the conductivity of compressed molded specimens with the same amount of CB particles only increased by two orders of magnitude **(Figure 12b)**. The calculated percolation thresholds were 0.87 wt.% and 4.3 wt.% for SLS and compressed molded samples, respectively. These values indicate that the SLS approach has a greater advantage than the compression-molding process in improving the electrical properties of CB/PA composites.

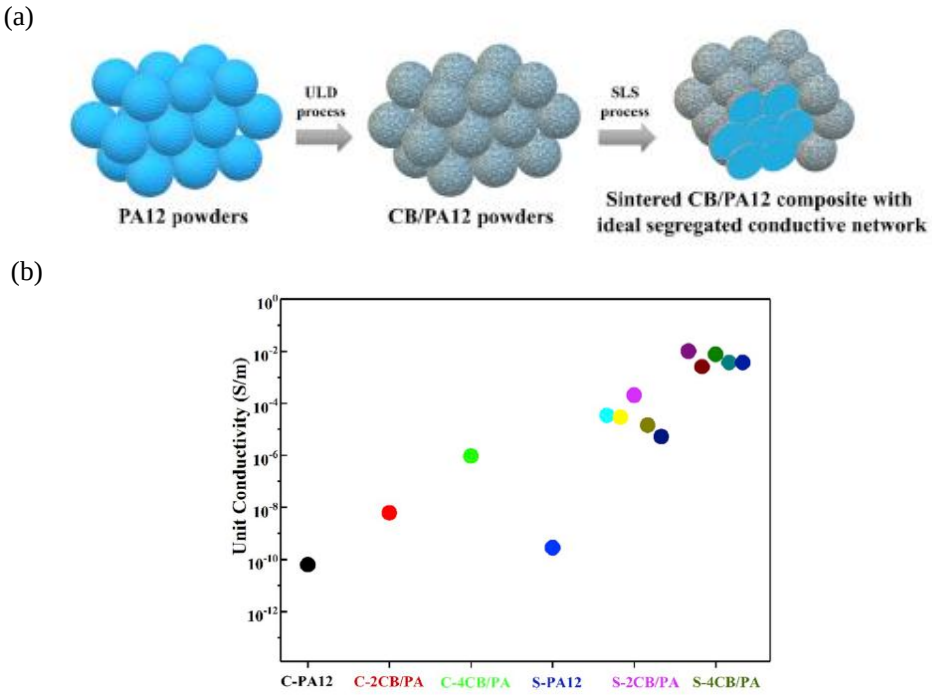

Figure 12. (a) Formation mechanism of the ideal segregated conductive network by ULD (ultrasonic-assisted liquid-phase absorption and deposition process), followed by SLS; (b) Electrical conductivity of compression-molded and SLS specimens with different CB

contents: C stands for compressed, S for sintered, the number is the wt.% of CB, and no number means pure PA12. Reproduced with permission from [70]. Copyright 2019, Elsevier.

Jayapiriya and Goel [71] studied the surface modification of two carbon/PLA bioelectrodes produced by FDM from commercially available conductive PLA composite filaments, named "Carbon Black" (CB, from Proto-pasta) and "Amolen Black" (AM, from Amolen company). Chemical treatments with dimethylformamide (DMF) or dichloromethane (DMC) for CB and AM, respectively, led to the production of a higher conductive area and hollow structures that increased the surface area available for enzyme immobilization. Optimized results were obtained by cyclic voltammetry (CV) in the presence of glucose, see **Figure 13**, with a maximum current density of 6.5 mA cm^{-2} and 0.38 mA cm^{-2} for CB bioanode and biocathode, respectively. Similarly, for the AM electrode, the maximum current density was 4.5 mA cm^{-2} and 0.1 mA cm^{-2} for the anode and cathode, respectively. Since no oxidation occurs in the absence of glucose, these results showed that adequate immobilization of the enzyme on both electrodes has occurred. Overall, the authors interpreted that the CB bioelectrodes was best suited for electrochemical devices than the AM electrodes.

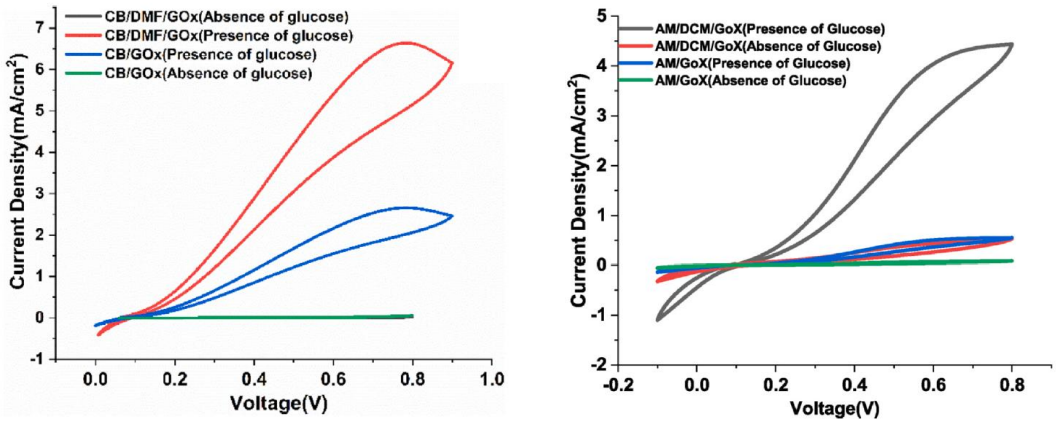

Figure 13. Cyclic voltammogram of 3D-printed bioelectrodes based on CB (left) and AM (right). Reproduced with permission from [71]. Copyright 2020, Elsevier.

Abdalla et al. [32] investigated the influence of 3D-printing parameters (layer thickness and print orientation) on the electron transfer kinetics of FDM-printed CB/PLA electrodes. Results are given for hexaammineruthenium (III) chloride redox species **(Figure 14)**. The increase in the print layer thickness resulted in a reduction in the voltammetric response (ΔE) and the electron transfer rate ($k°$) of the material, which were further reduced for horizontally printed layers (see **Figure 14b** and **Figure 14c**). In doing so, the authors provided keys insights for electrode design and fabrication.

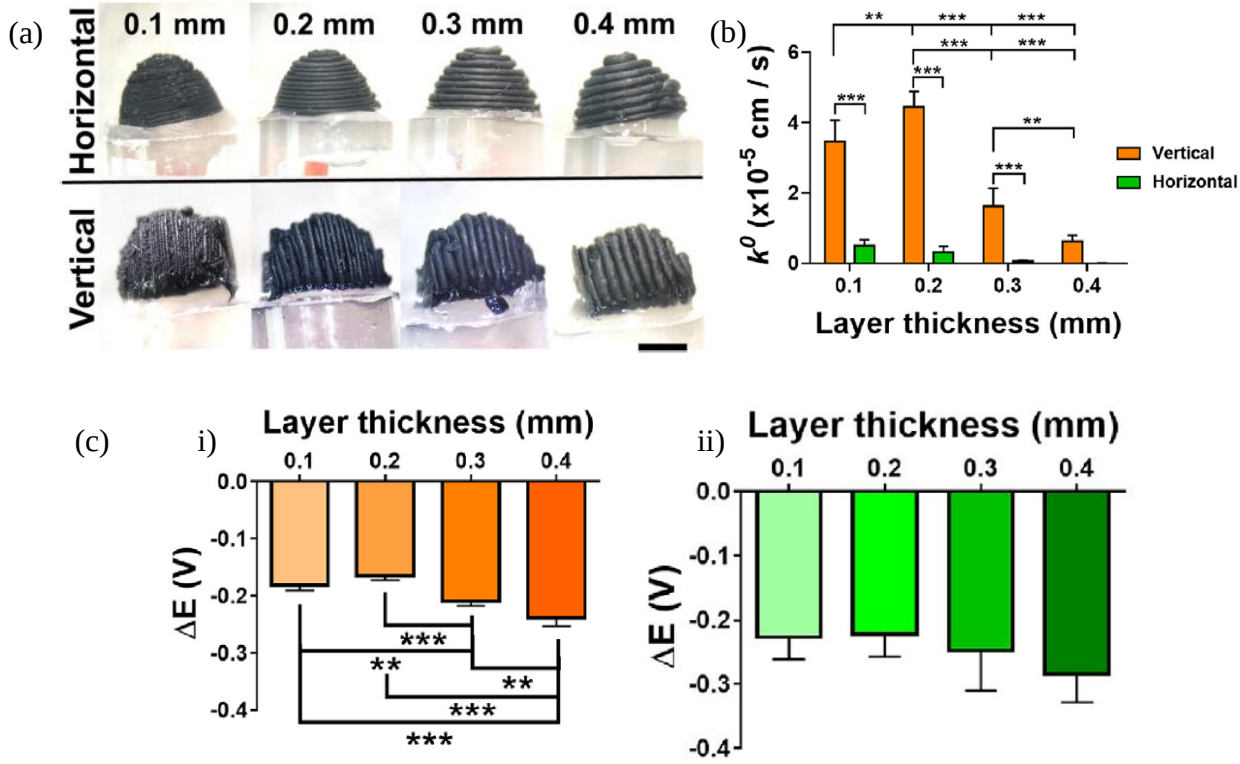

Figure 14. (a) Optical microscope side views of CB/PLA electrodes, 3D-printed in horizontal and vertical orientation with a layer thickness of 0.1 to 0.4 mm. The electrical connection is made vertically under the electrodes. The scale bar is 2 mm; (b) Electron transfer rate (k^0) from electrodes printed at various layer thicknesses; (c) Voltammetric response of hexaammineruthenium (III) (ΔE) from multiple electrodes of various layer thicknesses: (i) vertical electrodes, and (ii) horizontal electrodes. The data are presented as mean standard

deviation, *p<0.05, **p<0.01 and ***p<0.001. Reproduced with permission from [32]. Copyright 2020, Elsevier.

The development of 3D-printed graphene-based conductive composites is also very promising for electrochemical applications. Browne et al. [72] demonstrated that due to low graphene content (typically around 8 wt.%) and the insulating behavior of most thermoplastics, electrodes printed by FDM with a commercial graphene/PLA filament were mostly non-responsive to a range of electrochemical probes, including the $[Fe(CN)_6]^{4-/3-}$ redox system **(Figure 15)**. The treatment of the electrode with DMF followed by electrochemical activation (consisting of the application of a constant potential from 1.5 to 2.5 V vs. Ag/AgCl in phosphate buffer solution) resulted in improved electron transfer from the graphene/PLA electrode. The optimum was found for an activation time of 150 s, with the smallest peak separation value (ΔE_p) of 171 mV and the fastest heterogeneous electron transfer (HET) constant of 2.4×10^{-3} cm s^{-1}. In comparison, an electrode treated only with DMF had a ΔE_p of 527 mV and a HET of 2.13×10^{-5} cm s^{-1}. Thus, the authors have provided a simple method to prepare cost-effective, lab-made, highly electroactive graphene/PLA electrodes.

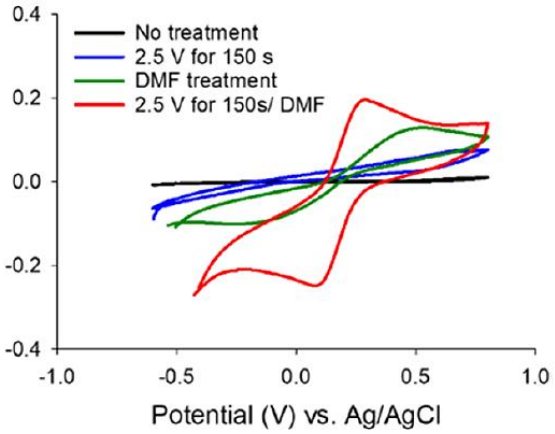

Figure 15. Effect of DMF and electrochemical treatments on a 3D-printed graphene/PLA electrode using the $Fe(CN)6]^{-4/-3}$ redox probe. Responses from untreated, electrochemically-treated only, DMF-treated only, and DMF/electrochemically-treated 3D electrodes are

compared. Reproduced with permission from [72]. Copyright 2018, American Chemical Society.

The potential of 3D printing, through the FDM technique has been extended to provide an affordable and efficient method for the production of electrodes and other micro-devices. The architecture and surfaces of these electrodes can easily be modulated to suit different applications, which gives 3D printing a considerable advantage. However, in some areas, such as where the printing orientation influences the performance of the electrodes or where a specific material is required, traditional manufacturing options remains a preferable option.

Graphene and graphene oxide are also well represented as carbon fillers for conductive electrode [73] or for various other applications. Indeed, De Leon et al. [74] have developed an easy method for printing by SLS a conductive graphene/polyamide powder (PA) suitable for electrostatic metal-free motors. The conductive powder was prepared by depositing graphene oxide (GO) nanosheets on PA particles in water, followed by chemical reduction into reduced graphene oxide (rGO), thereby producing electrical conductivity **(Figure 16a)**. Both pure PA and GO-PA are non-conductive, while the conductivity (measured on pressed pellets) increases with rGO loading **(Figure 16b)** to a value of 10.5 $S.m^{-1}$ for pure rGO pellets. The calculated percolation threshold value was very low, about 0.05 vol.%, but it allowed the rGO nanosheets to form a network throughout the pellet, enabling the passage of current to illuminate a LED **(Figure 16c)**.

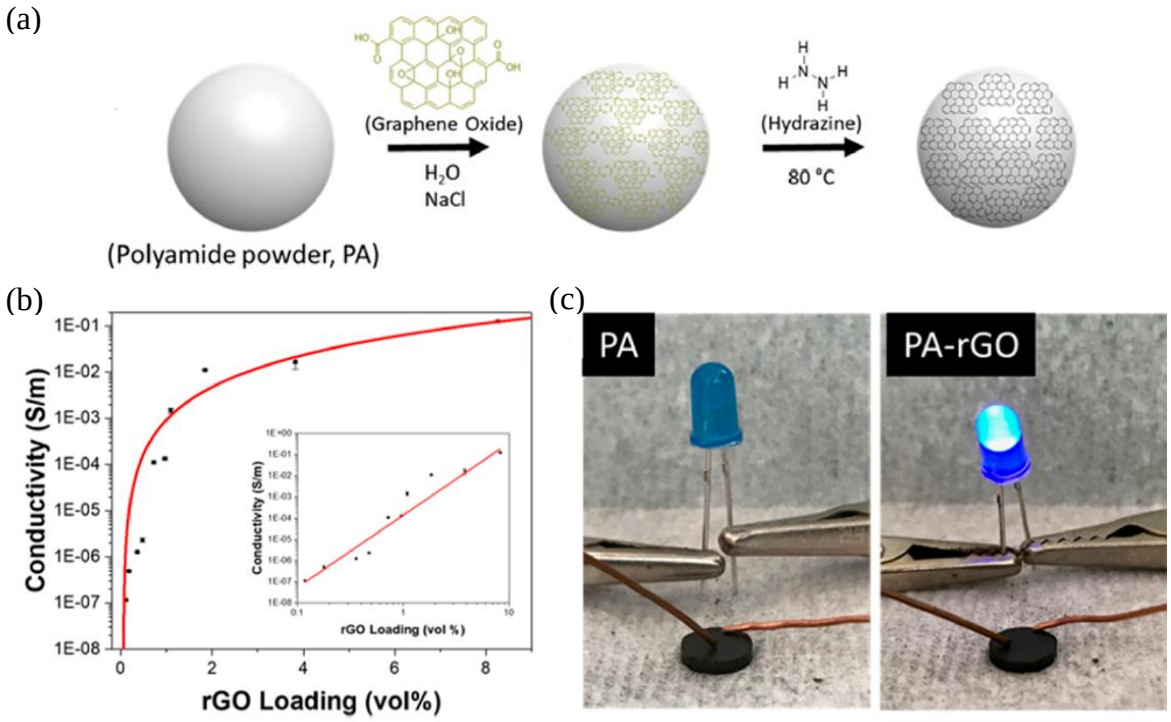

Figure 16. (a) Schematic representation of the preparation of a conductive powder by bonding GO to the surface of PA particles and reducing it with hydrazine, to be subsequently pressed into pellets or printed by SLS method; (b) Electrical conductivity of pressed pellets vs. rGO loading in semi-log scale; (c) Photographs of pressed pellets of PA and PA-rGO as part of an electrical circuit to light up a LED. Reprinted with permission from [74], Copyright 2018, American Chemical Society.

Carbone nanotubes (CNTs) are also widely used as conductive filler in 3D-printing technologies. Intending to develop a strain sensing device, Luo et al. [75] presented a direct ink writing (DIW) technique for printing a custom-made conductive ink composed of colloidal MWCNTs (7 wt.%) embedded in PDMS, a bi-component (base A + crosslinker B) silicone elastomer. Details on the DIW technique are available in the Supplementary Information. A cubic woodpile structure (20 × 20 × 10mm) was printed, and its performance was characterized. The resistance between the top and bottom faces was found to be 90 Ω, demonstrating good electrical conductivity (as pure PDMS is insulating). This resistance

progressively decreased with the increase of the weight (from 20 to 200 g) applied on the surface of the structure **(Figure 17b)**. Thus, the material could be applied in strain and pressure sensing devices, such as miniature electrothermal actuators.

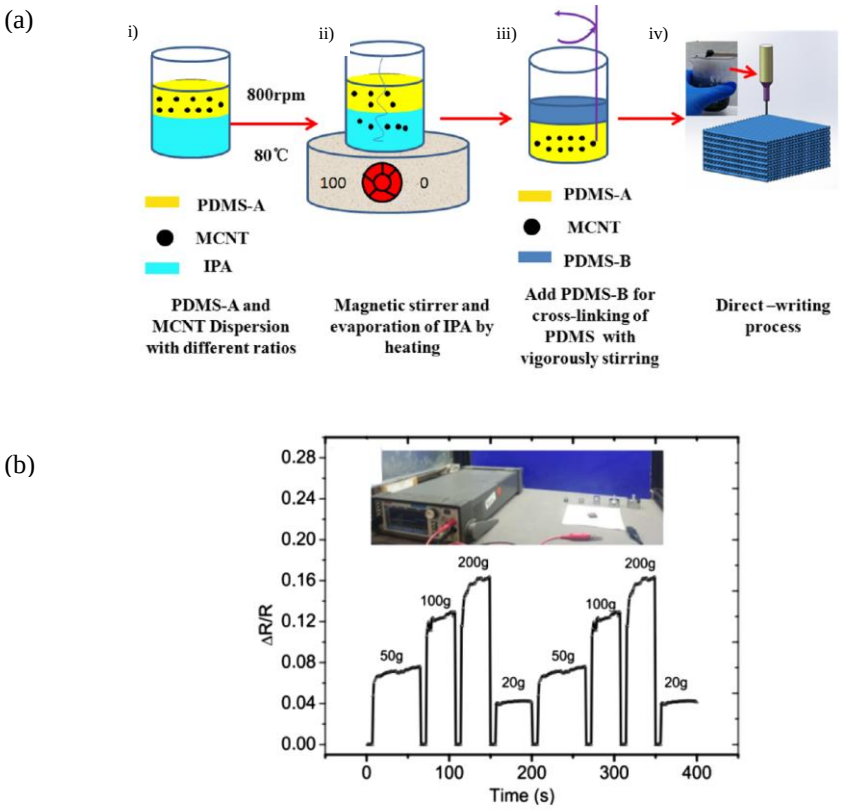

Figure 17. (a) Scheme of the experimental ink preparation and the direct writing processes: (i) mixing of MWCNTs and part A of PDMS in isopropyl alcohol (IPA), (ii) evaporation of IPA by mechanical stirring and heating, (iii) preparation of the CNT/PDMS composite by thorough mixing with the crosslinker (part B of PDMS), (iv) DIW process using the CNT/PDMS composite; (b) Change in the resistance of the woodpile structure under different applied weights. Reprinted in parts with permission from [75]. Copyright 2018, American Chemical Society.

Li et al. [76] have proposed SWCNTs and graphene nanoplatelets (GNPs) as fillers in polyimide (PI) to make piezoresistive strain sensors. The inkjet printing technique, the details of which are available in the Supplementary Information, was used to produce a conductive

structure with filler contents close to the percolation threshold, from 1.2 - 2.0 wt.% and 1.0 - 1.8 wt.% for CNTs and GNPs, respectively. The sensitivities of the piezoresistive nanocomposite strain sensors were evaluated using the gauge factor (GF), i.e., the ratio of the change in resistance to the strain. Optimal compositions of 1.8 wt.% CNT in PI and 1.4 wt.% GNP in PI were suggested for a maximum GF of 3.5 and 26, respectively **(Figure 18)**. The GNP-PI sensors exhibited higher strain sensitivity than their CNT-PI counterparts, while they were slightly more sensitive to temperature. Both nanocomposites proved to be very promising for flexible strain sensors.

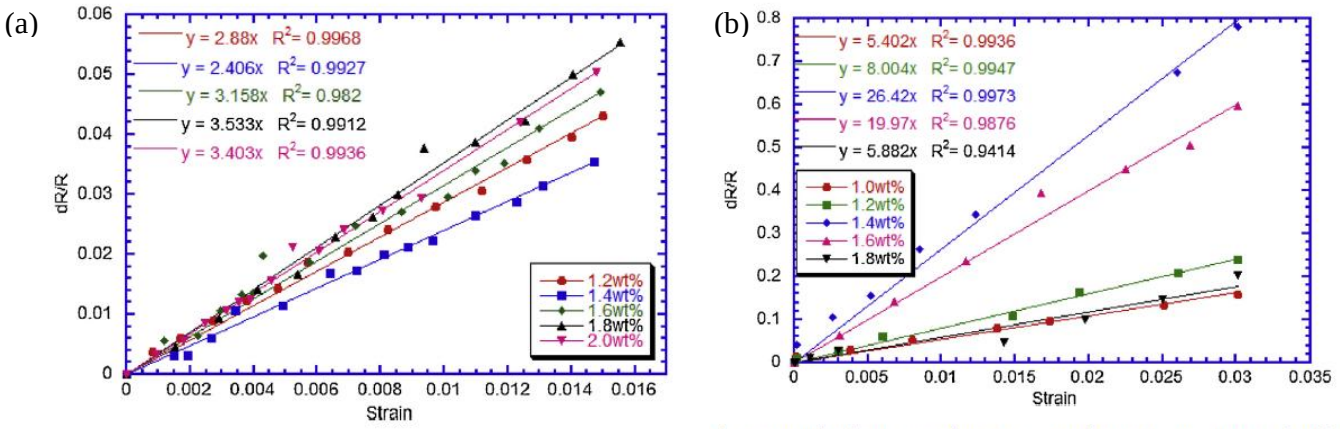

Figure 18. Change in normalized resistance as a function of strain for nanocomposites: (a) CNT-PI; and (b) GNP-PI. Reproduced with permission from [76]. Copyright 2019, Elsevier.

Conductive nano-woodpiles structures were developed by Staudinger et al. [77] via two-photon polymerization (TPP) with the printing of a commercial photosensitive inorganic-organic hybrid material, Femtobond, with SWCNTs as a conductive filler. Details on the TPP technique are available in the Supplementary Information. Two types of commercial SWCNTs, long (Tuball, length greater than 5 µm and diameter of 1.6 nm) and short (Nanoamor, length from 1 to 3 µm and diameter of 1.1 nm) were compared. It was found that the surface electrical resistivity of nanocomposite films was dependent on the type of SWCNT: the nanocomposite containing Tuball SWCNTs had low resistivity values of 4.6 ×

10^5 Ω sq^{-1} for a SWCNT content of 0.01 wt.%. In contrast, the nanocomposite containing Nanoamor SWCNTs required 2 wt.% of SWCNT to achieve a resistivity value of 1.5×10^6 Ω sq^{-1}. The obtained microstructures exhibited small conductive areas with values of contact currents between 20 and 500 nA **(Figure 19a)**. However, the agglomeration of SWNCTs (even at low Tuball contents) negatively influenced the electrical conductivity and in many cases did not result in any current. TPP is thus a promising process for the design of nanocomposites, but further optimization of CNTs dispersion and microstructure control is needed (see **Figure 19b**).

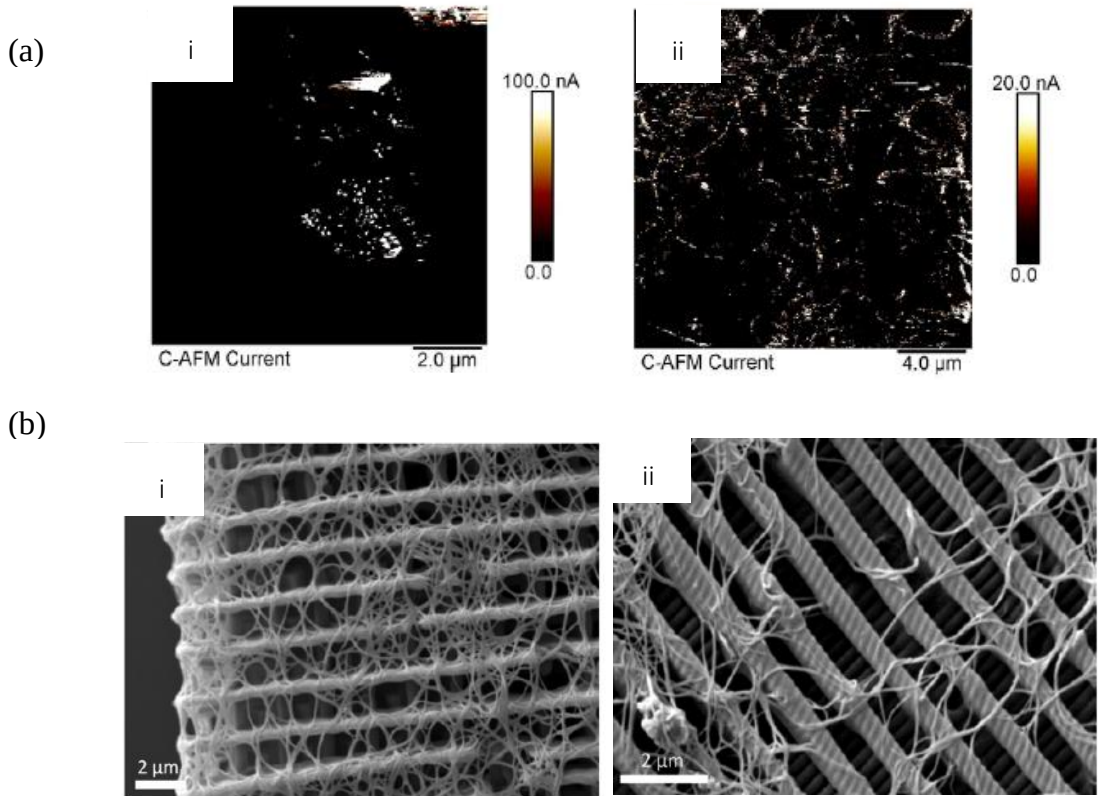

Figure 19. (a) Contact current signal measured by AFM on microstructures containing: (i) 3 wt.% Nanoamor CNTs, or (ii) 0.05 wt.% Tuball CNTs; (b) 3D woodpile microstructures fabricated by TPP (laser power 30 mW, laser scanning speed 50 µm s^{-1}) from Femtobond/SWCNT dispersions with 0.05 wt.% Tuball CNTs sonicated for: (i) 10 min, and (ii) 20 min. Reproduced with permission from [77]. Copyright 2017, Elsevier.

Liu et al. [78] designed MWCNT-thiol-acrylate composite resin compatible with TPP, with MWCNTs concentrations up to 0.2 wt.%. Thanks to a uniform MWCNT distribution in the resin, the 3D-printed nanostructures showed improved electrical and mechanical properties allowing a wide range of applications, including integrated photonics. Indeed, the electrical conductivity of the composite resin increased by more than 11 orders of magnitude to 46.8 S m^{-1} with the addition of 0.2 wt.% CNT, when the hardness of the cured resin increased from 43 to 67.5 kPa with 0.1 wt.% CNT content. Thus, recent development in nanoscale printing has opened up the possitibility of improving miniaturized devices.

3.3 Microwave absorption properties

Great attention has been paid to microwave-absorbing materials, and the application of 3D printing technology simplifies their design. Zuo et al. [79] reported on a new microwave-absorbing nanocomposite material using Digital Light Processing (DLP) of graphene/carbonyl iron powder/polymethyl methacrylate (G/CIP/PMMA). Details on the DLP technique are available in the Supplementary Information. The materials for DLP were prepared by mixing photocurable PMMA resin with different amounts of microwave-absorbing powder. The complex permittivity and complex permeability of the printed composites were recorded in the frequency range of 2 to 18 GHz. The dielectric properties, electrical loss, and reflectance values increased significantly with the graphene content **(Figure 20)**. The addition of graphene enhanced the microwave reflection loss capability, facilitating the conversion of electromagnetic energy into heat (or other forms of energy), and resulted in the dissipation of microwaves, thus improving the absorption properties of the material.

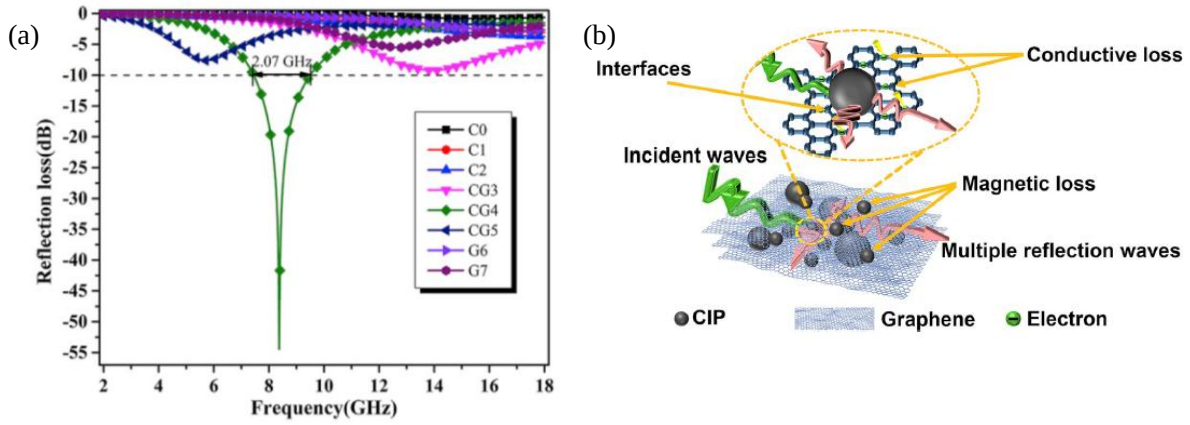

Figure 20. (a) Reflection loss of the sample produced by DLP at a thickness of 2.1 mm. C: carbonyl iron, G: graphene; 1-7: slurries of different compositions (no carbon for C0-C2, increase in carbon content for slurries CG3 to CG5, and G6-G7); (b) Schematic diagram of the microwave absorption mechanism of the graphene/CIP/PMMA composite. Reproduced with permission from [79]. Copyright 2019, Elsevier.

3.4 Biocompatibility

Finally, the incorporation of carbon particles in a matrix can lead to special properties. Recently, Cui et al. [80] applied a 3D-printed gel filled with CNTs to bone regeneration. They endowed a polyion complex hydrogel (PIC, obtained by polymerization of polystyrene sulfonate as anionic monomer and poly(methacryloylamino)propyl-trimethylammonium chloride as cationic monomer) with a bioactive ability with MWCNTs (at a content of about 3 wt.%), known to be osteoconductive agents. The resulting scaffolds were characterized by highly interconnected porosity with desirable mechanical performance as they returned to their initial state after compression. They led to better promotion of the osteogenic effect than scaffolds without CNTs **(Figure 21)**, simultaneously promoting osteogenesis and angiogenesis, thus opening up new perspectives for custom bone tissue engineering.

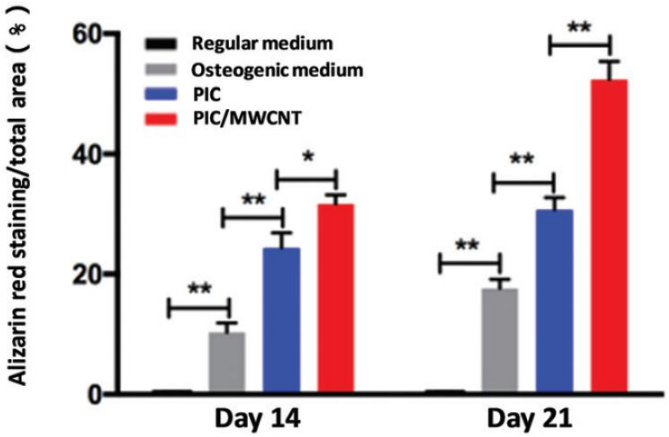

Figure 21. Average area of stained mineralized matrix after 14 and 21 days incubation, a high area indicating a high osteogenic induction. Reproduced with permission from [80]. Copyright 2019, Royal Society of Chemistry.

4. 3D printing of pure carbon materials and their precursors

3D printing to obtain pure carbon objects – not just carbon-filled composites – is a newer but rapidly developing field. Significant research efforts have been devoted to the design and synthesis of new carbon materials from different printable precursors.

4.1 3D printing as a step in the process of preparing new carbon objects

In the limited context of 3D printing, carbon materials can be prepared by various techniques including reduction of graphene oxide, pyrolysis of carbon precursors, or carbon deposition on 3D-printed hard templates such a polymer preforms. Thus, combining the versatility of 3D-printing and carbonization allows tailor-made carbon materials to be obtained in a multi-stage process. Porous carbon materials have been intensively studied because of their inherent advantages such as high surface area, electrical conductivity, and chemical stability. As detailed below, such porous carbon can be obtained by printing and

pyrolyzing a GO gel, using a printed sacrificial template, or pyrolyzing a printed carbon precursor [81].

4.1.1 Pyrolysis of a structure based on GO gel

Zhang et al. [82] coupled multi-nozzle drop-on-demand inkjet printing of a suspension of pure graphene oxide with freeze casting for rapid printing of 3D architectures. An aqueous solution of GO (about 10 mg L^{-1}) was rapidly frozen on a cold sink. When the liquid solution is deposited on top of the previously frozen material, the frozen surface melts, then the two materials mix and refreeze together almost immediately, hence producing the successive layers. The obtained structures were freeze-dried and thermally annealed at 1000 °C in argon atmosphere, resulting in ultra-lightweight 3D graphene aerogels (GA) **(Figure 22a)**. These printed GAs had a typical semiconductor behavior with a negative temperature coefficient, i.e., the relative electrical resistance ($\Delta R/R$ in %) increased to +97 % when decreasing the temperature from room temperature to -190 °C and dropped to -48 % when increasing the temperature from RT to 350 °C. High electrical conductivities, ranging from 2.2 to 15.4 S m^{-1} at room temperature for GA at densities ranging from 0.5 to 10 mg cm^{-3}, have also been measured. The mechanical properties indicated that the aerogel can withstand up to 16,000 times its own weight and can elastically deform up to 50% **(Figure 22b)**. The 3D-printed GAs presented in this work were stiffer than their counterparts such as conventional (bulk) GA, thus promoting future applications for strain sensors.

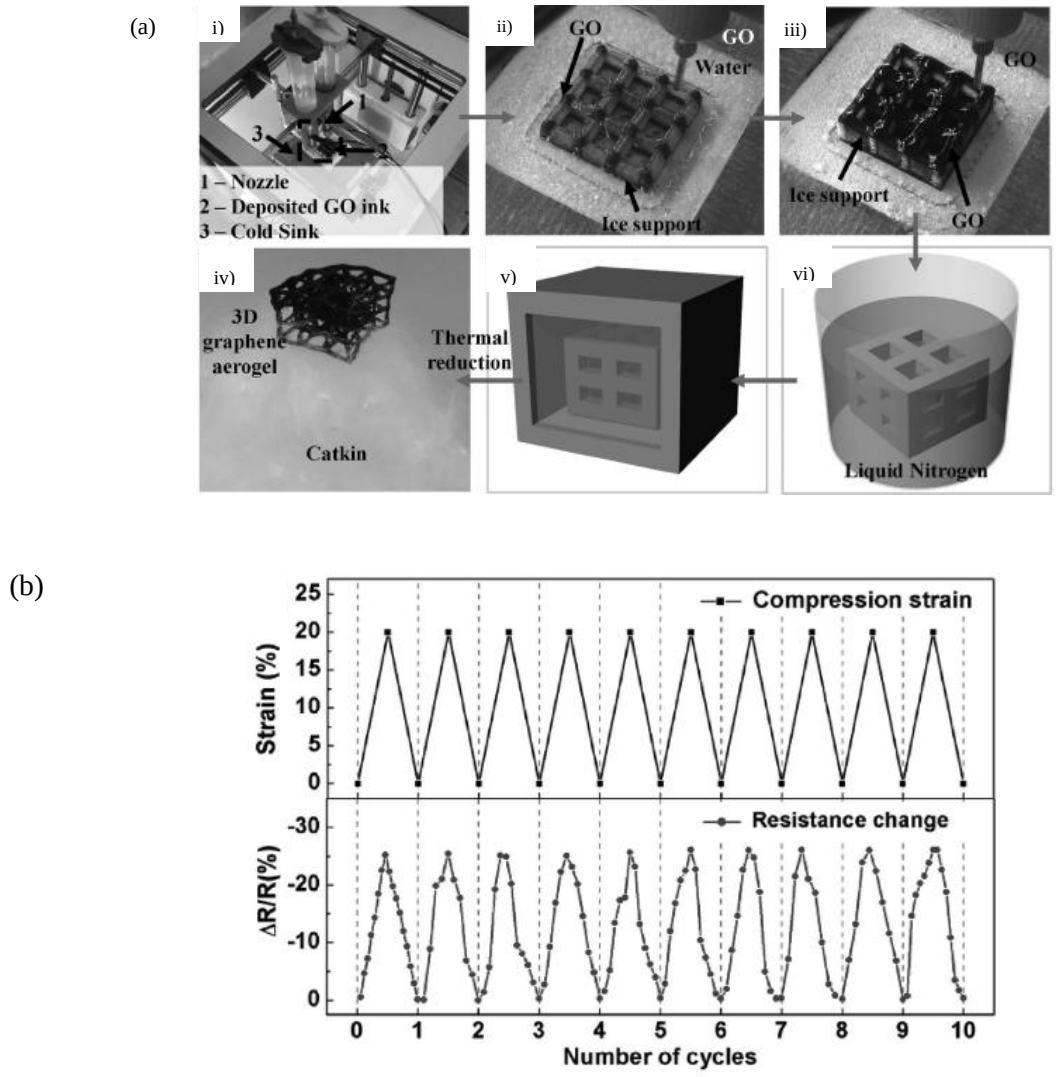

Figure 22. (a) Production of graphene aerogel (GA) by 3D printing: (i) printing setup, (ii) 3D printing of GO suspension on an ice support, (iii) 3D printing of successive layers of GO suspension, (iv) immersion of the printed ice structure in liquid nitrogen, (v) freeze-drying, (vi) ultra-lightweight GA on a catkin, after thermal reduction at 1000 °C; (b) Resistance changes according to the compression cycles of the printed GA. Reproduced with permission from [82]. Copyright 2016, Wiley-VCH.

Similarly, Peng et al. [83] presented an ink-based 3D printing strategy for the construction of ultra-lightweight 3D biomimetic hierarchical graphene materials (BHGMs). A printable ink based on partially reduced graphene oxide (pr-GO) was developed using ascorbic acid (used

as a mild reducer for GO) and GO sheets with a lateral size of about 5 nm. By combining the printing process with freeze-casting treatment (freezing of the slurry to induce a repetitive pattern of growing solvent crystal along the freezing direction and associated rejection of particles between these crystals, usually followed by the sublimation of the solvent), pr-GO was able to form microscopic cellular structures. After drying and thermal reduction at 1100 °C, the cellular microstructures were preserved in the form of graphene "filaments" and formed ultra-light BHGM structures **(Figure 23a)**. These structures exhibited superelasticity at a low density of 8.5 mg cm^{-3} as their Young's modulus remained at 90.1 % of its original value after cyclic compression of 95 % strain under 66 kPa, and they were able to withstand 22,000 times their own weight without irreversible deformation.

Triboelectric nanogenerators (TENGs) based on these 3D-printed BHGMs with a contact separation mode (fluorinated ethylene propylene as the triboelectric layer and aluminum foil as the contact layer to create the charge imbalance in the TENG) generated high voltages under compression. Indeed, the voltage difference at open circuit (V_{oc}) increased from 56.3 to 117.6 V from 0 to 45 % compression, and the short-circuit current (I_{sc}) increased from 0.12 to 0.29 µA with an increase in compression ratio between 0 and 75 % (values at 0 % of compression were taken when contacting the Al foil and the triboelectric layer). At 75 % compression at different operating frequencies, the open-circuit voltage remained unchanged (about 114.5 V), but the short-circuit current rose from 0.23 to 1.48 µA at 0.5 and 2.5 Hz, respectively **(Figure 23b)**. The authors demonstrated that BHGMs are efficient and elastically deformable electrodes that can be successfully applied to nanogenerators.

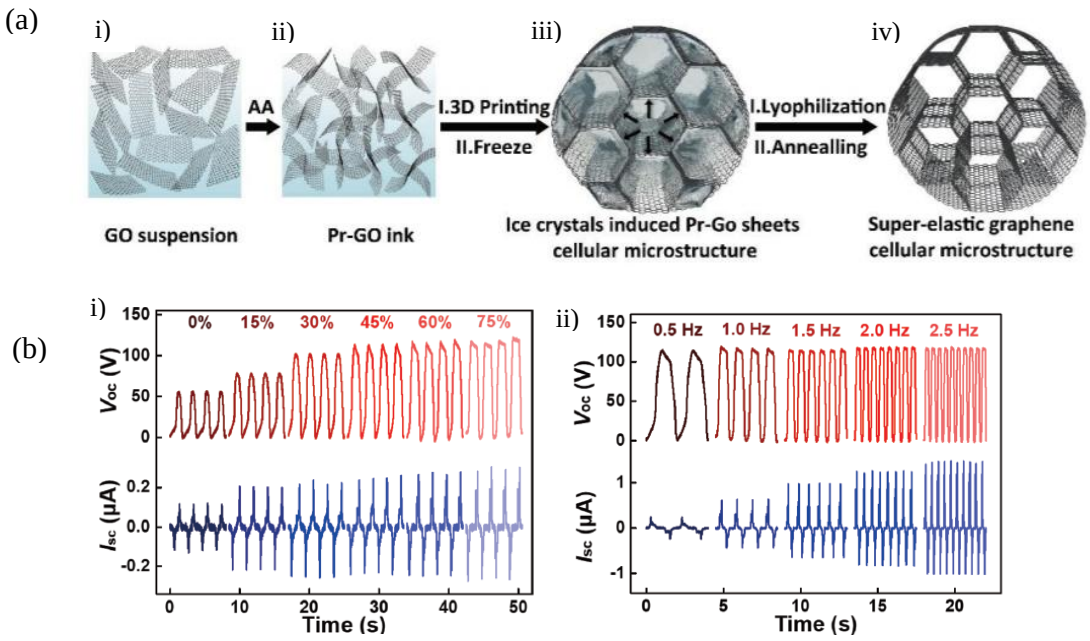

Figure 23. (a) Diagram of the formation of a super-elastic graphene-based conducting structure: by using pr-GO ink (i and ii), printed materials can have a microscopic cellular structure with ice as template during the freeze-casting process (iii), leading to a super-elastic graphene cellular microstructure after annealing (iv); (b) V_{oc} and I_{sc} of the TENG under: (i) various compression ratios ranging from 0 % (at the contact point between triboelectric layer and Al foil) to 75 %, and (ii) various motion frequencies ranging from 0.5 to 2.5 Hz. Reproduced with permission from [83]. Copyright 2019, Wiley-VCH.

In addition to requiring time-consuming preparation methods, GO-based carbon materials do not always have the appropriate electrical conductivity. However, this multi-stage printing and then pyrolysis process can also be applied to polymer templates to obtain highly porous carbon materials.

4.1.2 Printed structure as sacrificial template

Szczurek et al. [35] proposed a template method based on thermoset polymer periodic lattices to form, via hydrothermal treatment followed by pyrolysis, a carbon periodic cellular architecture. Preforms were first produced by stereolithography of photocurable resin (SLA,

details of which are given in the Supplementary Information) and were next coated with a hydrochar formed from an aqueous resorcinol/formaldehyde solution under hydrothermal conditions, and finally pyrolyzed at 1000 °C **(Figure 24)**. The authors proved the need for nickel nitrate as a graphitization catalyst to improve carbon yield and reduce struts deformation, leading to isotopic shrinkage and solid struts. The structure was converted to a periodic glasslike carbon lattice (carbon yield of about 20 %), stiffer than typical carbon foam, and having excellent electrical conductivity (between 1200 and 2000 S m^{-1}). The materials were found to behave like photonic crystals in the GHz-THz range to provide perfectly tunable resonant absorption for the intended application [84].

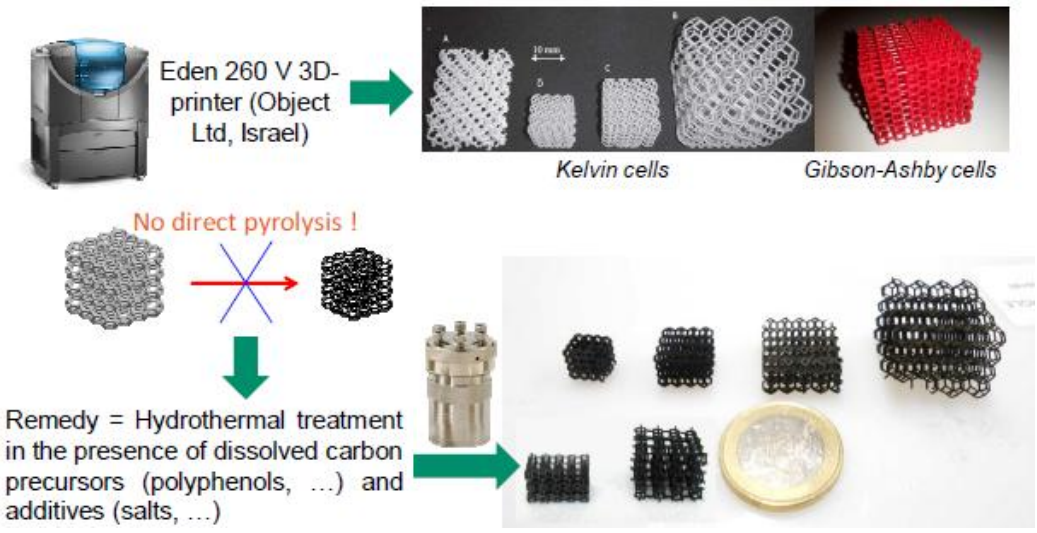

Figure 24. General preparation scheme of polyphenol/formaldehyde-based periodic carbon structures, based on templates produced by SLA. Reproduced with permission from [81]. Copyright 2020, Elsevier.

Also using a sacrificial polymer template, Chen et al. [85] studied the fabrication of carbon cellular microstructures (CCMs) using the SLA process. A foam-like template **(Figure 25a)** was printed with acrylic/epoxies photo-resin, then coated with a mixture of NaCl (granular support) and graphite powder (improving the mechanical and electrical properties) and finally carbonized at 600 °C under argon. The resulting carbon structures were then pyrolyzed at

1000 °C under argon to obtain low-shrinkage CCMs. The volume shrinkage increased to 52 % with the graphite content up to 4 wt.%, which remained extremely low compared to other cellular periodic carbon reported, with a shrinkage between 70 and 85 % **(Figure 25b)**, or compared to non-coated polymers with polymer shrinkage of 90 %. Nevertheless, the electrical conductivity, with a maximum value of 0.43 S cm^{-1}, was found to be lower than that of graphitized microporous carbon foams (1.70 S cm^{-1}) having a close bulk density of 0.03 g cm^{-3}.

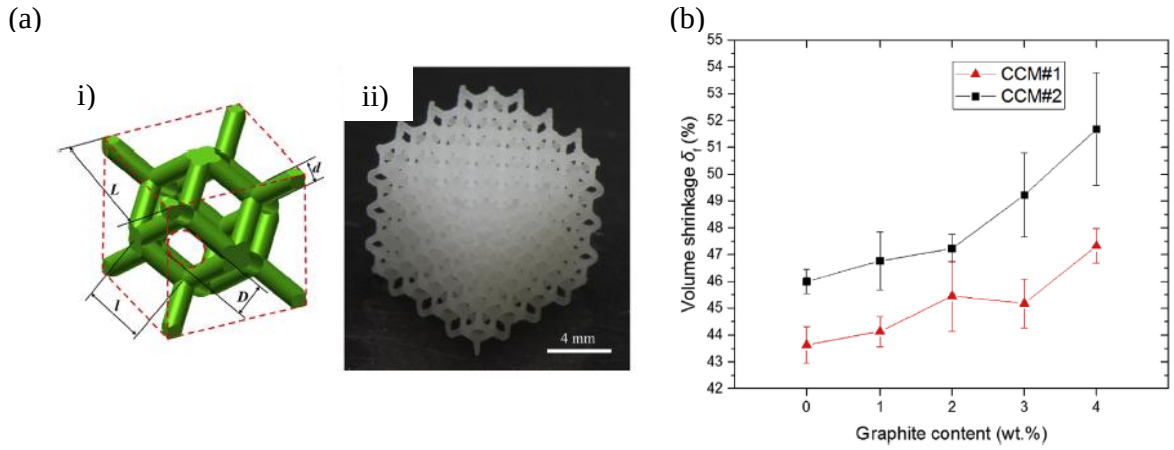

Figure 25. (a) Polymer architecture produced by SLA; (b) Volume shrinkage of the CCM at different graphite contents after the full process. Reproduced with permission from [85]. Copyright 2017, Elsevier.

In most cases, thermoplastics and resins used in 3D-printing technologies have nearly zero carbon yield or undergo significant volume shrinkage after pyrolysis. Thus, the template method was found to be feasible and simple to obtain highly porous carbon from polymer preforms with extremely low carbon yields upon direct pyrolysis. This method allows stabilising the complex structure of such preforms, which can only be produced by 3D printing.

To significantly reduce the number of steps, researchers mainly turned to direct pyrolysis of 3D-printed carbon precursors.

4.1.3 Pyrolysis of a printed carbon precursor structure

Ge et al. [86] studied a nanostructured resorcinol-formaldehyde ink for direct 3D writing. A formaldehyde/resorcinol ink with non-Newtonian behavior was printed, cured by the action of a spray of 34.5 wt.% HCl aqueous solution, then dried with supercritical CO_2 (to form a resorcinol/formaldehyde aerogel, RFA) and finally pyrolyzed at 1000 °C to obtain a 3D-printed carbon aerogel (CA). Both RFA and CA samples had pores at the millimeter scale, at the micron scale, and a porous skeleton at the nanoscale and presented a specific surface area of 631 and 265 $m^2\ g^{-1}$, respectively. The 3D-printed CA exhibited a large number of small mesopores (3.7 nm) that played a significant role in the adsorption of phenol red indicator (molecule size of about 2 nm) when immersed in a phenol red-stained cell medium. Indeed, the CA samples were able to adsorb 90% of the phenol red indicator (initial concentration of 8.1 $mg.L^{-1}$) while the RFA and the wet RF gel adsorbed only 60 % and 40 % of the indicator, respectively. The high adsorption capacity of the phenol red-stained cell medium and the non-toxic nature of the CA therefore suggests its possible to cell engineering.

Steldinger et al. [33] have developed a new method for obtaining porous, hierarchically structured carbon based on the SLA process. A photocurable resin composed of PETA (pentaerythritol tetraacrylate), DVB (divinylbenzene, as an aromatic monomer to improve carbon yield), and a liquid porogen mixture (either diisodecyl phthalate, DIP, or dioctylphtalate, DOctP) was prepared to print a porous polymer monolith **(Figure 26a)**. After extraction of the porogen, the structure was oxidized in air at 300 °C (6 h, heating ramp 10 K min^{-1}) then pyrolyzed at 900 °C under N_2 atmosphere (heating rate of 3.3 K min^{-1}). While burn-offs were relatively identical (68-70 %), the pore structure and porosity of the monoliths were highly dependent on the type and content of the porogen: the use of 30 vol.% of DIP resulted in a pore diameter of 155 nm (which reduced to 30 nm with 20 vol.% porogen), while the use of 30 % of DOctP resulted in a pore diameter of 81 nm. Although the pyrolyzed

structure showed some microporosity, CO_2 activation (between 860 and 900 °C) was used to increase the specific surface area, allowing an increase from 536 m^2 g^{-1} (pore volume of 0.29 cm^3 g^{-1}) for non-activated carbon to 2200 m^2 g^{-1} (pore volume of 1.68 cm^3 g^{-1}) at the highest burn-off **(Figure 26b)**. The authors thus demonstrated a flexible and fast printing method, with high final carbon yield and controlled porosity that can be applied to multiple fields.

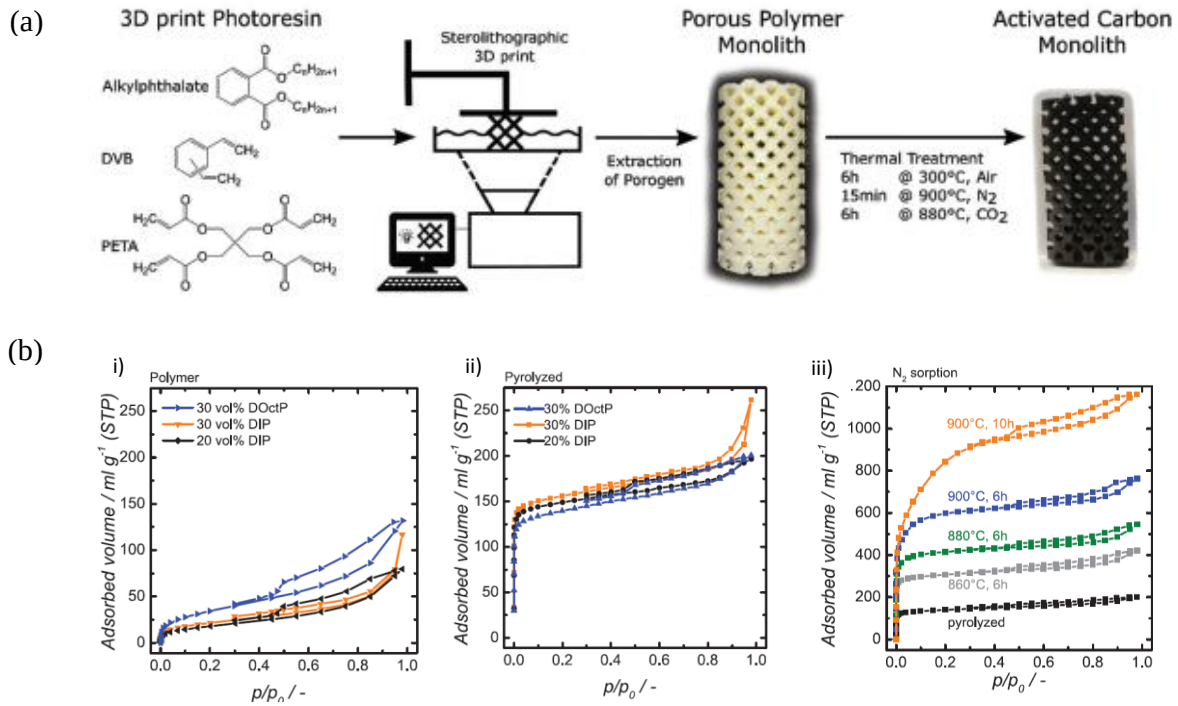

Figure 26. (a) Schematic overview of the 3D-printing process starting from a liquid photoresin, then producing a porous open-cell polymer structure (tetragonal unit cell) by SLA and subsequent extraction of the porogen phase, to finally obtain an activated carbon monolith with open cell structure after heat treatment consisting of stabilization in air, pyrolysis in nitrogen and activation by CO_2; (b) N_2 adsorption isotherms of: (i) extracted polymers, (ii) pyrolyzed carbon, (iii) printed carbon with 30 vol.% DOctP after pyrolysis and CO_2 activation at temperatures ranging from 860 to 900 °C. Reproduced under terms of Creative Commons Attribution license from [33]. Copyright 2019, published by Wiley-VCH.

The structures obtained with a high final carbon yield and increased porosity can easily be applied to electrochemical applications. Bian et al. [87] studied a 3D-printed porous carbon anode to improve power generation in microbial fuel cells **(Figure 27a)**. Different anode structures (same diameter and thickness but different pore sizes) were printed by a DLP process with a UV-curable photoresin and then carbonized to 800 °C under N_2 atmosphere, leading to a highly porous (about 95 %) anode material with good electrical conductivity and excellent biocompatibility. The highest maximum output voltage, open circuit potential, and power density were obtained for a pore size of 300 µm: 453.4 mV, 1256 mV, and 233.5 mW m^{-2}, respectively. These performances were superior to those of an 80 % porous carbon cloth anode (188 mV, 669.35 mV, and 69 mW m^{-2}) under the same conditions **(Figure 27b)**. The total resistance of the 3D-printed anode and the carbon cloth anode was almost the same, but a lower solution resistance of the 3D-printed anode demonstrated better mass transfer, indicating better nutrient accessibility for bacterial growth. Overall, the combination of 3D printing and the carbonization approach is a promising technique for studying low-cost, high-potential microbial fuel cells.

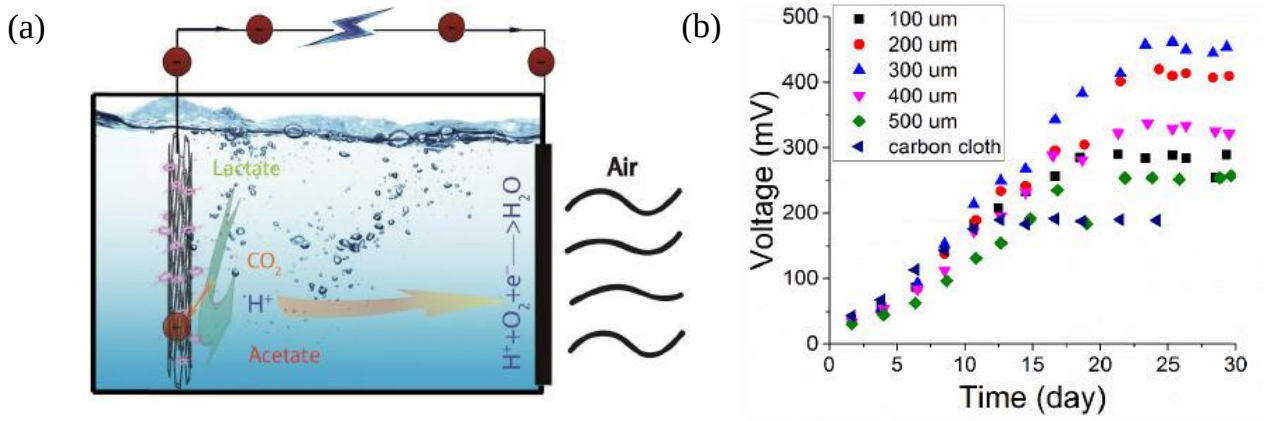

Figure 27. (a) Scheme of an air-cathode microbial fuel cell (MFC) configuration; (b) Voltage generation of MFCs with a carbon cloth anode or with 3D-printed carbonaceous porous

anodes with pore sizes of 100 – 500 µm. Reproduced with permission from [107]. Copyright 2017, Elsevier.

Recently, Rezaei et al. [88] have implemented a fast and simple approach to generate 3D carbon electrodes with a specified and controllable architecture using SLA printing technology followed by pyrolysis **(Figure 28a)**. Commercially available photoresins were investigated as carbon precursors under different pyrolysis conditions. No significant differences in chemical composition were noted between electrodes with fast and gradual pyrolysis at different temperatures (900 °C or 1000 °C under N_2 atmosphere). Cyclic voltammetry (CV) and electrochemical impedance spectroscopy (EIS) response experiments with $[Fe(CN)_6]^{-3/-4}$ as a redox probe showed higher oxidation and reduction peaks currents and lower charge transfer resistance for the rapidly pyrolyzed carbon electrode with a value of 5.03 Ω (at 1000 °C versus 7.32 Ω for the gradually pyrolyzed electrode at the same temperature, **Figure 28b**). These results were explained by the high specific surface area and high porosity of the structure, as the total BET area and pore volume were found to be 20 m^2 g^{-1} and 0.021 cm^3 g^{-1}, respectively, which are twice as high as those of the gradually pyrolyzed electrode (11 m^2 g^{-1} and 0.012 cm^3 g^{-1}, respectively). Thanks to their structural properties, a key factor influencing electrochemical performance, and the possibility of designing different complex structures, these 3D-printed carbon electrodes are promising for a broad range of applications.

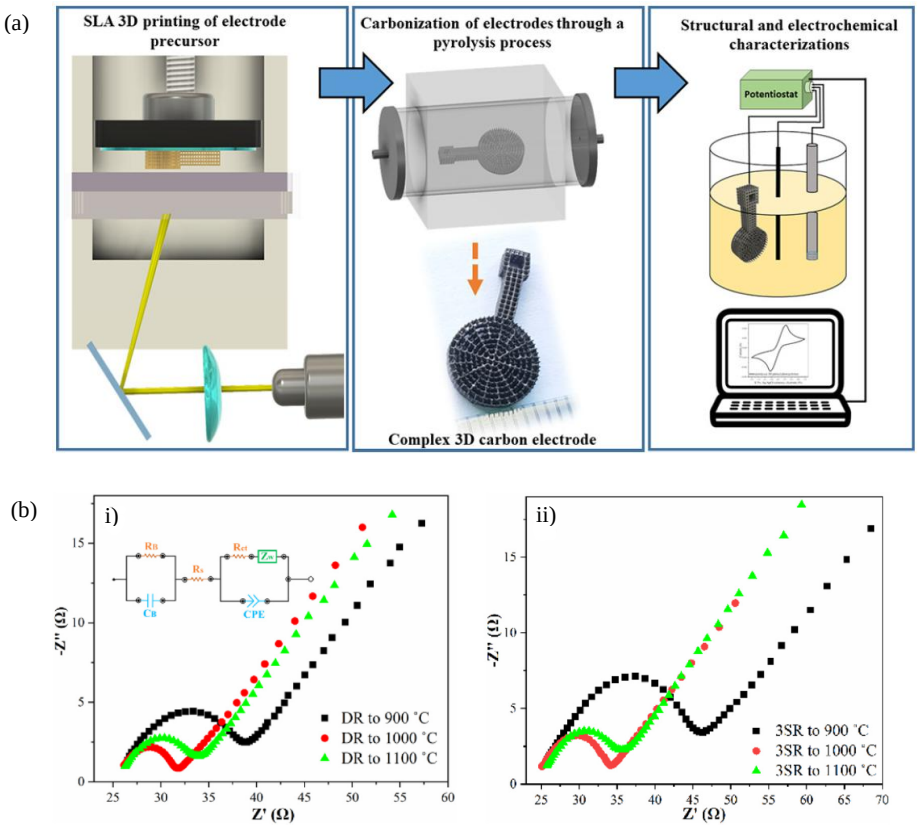

Figure 28. (a) Schematic procedure for producing an SLA-printed carbon electrode; (b) Impedance spectra of pyrolytic 3D carbon electrodes obtained with (i) fast (DR), and (ii) gradual (3SR) pyrolysis conditions and different final carbonization temperatures. Reproduced under terms of CC-BY license from [88]. Copyright 2020, Published by Elsevier.

Wang et al. [89] also proposed a method combining SLA, pyrolysis, and chemical activation to produce porous electrodes. A photosensitive resin was used as polymer precursor, and several structures with different pore diameters and shapes were printed and then slowly pyrolyzed **(Figure 29a)**. Chemical activation was performed with KOH, leading at 960 °C to a pore volume and BET area of 0.206 cm^3 g^{-1} and 101 m^2 g^{-1}, respectively, both higher than those obtained at 860 °C, 0.018 cm^3 g^{-1} and 8 m^2 g^{-1}, respectively. The electrochemical performance of the electrodes obtained was found to be 5.85 times higher in peak current density than that of carbon papers. They were thus tested in a supercapacitor and

a vanadium redox-flow battery. The specific capacitance obtained, around 30-40 F g^{-1}, was highly dependent on the specific surface area and the pore wall thickness and was lower than that of other carbon supercapacitors due to a non-optimized activation step **(Figure 29b)**. The application in vanadium redox-flow battery showed that superior diffusion performance (and a maximum electrolyte utilization of about 65.5 %) resulted from the minimum thickness and maximum porosity of the carbon matrix. The authors thus demonstrated a manufacturing method with a better understanding of the structure/performance relationship for producing carbon electrodes.

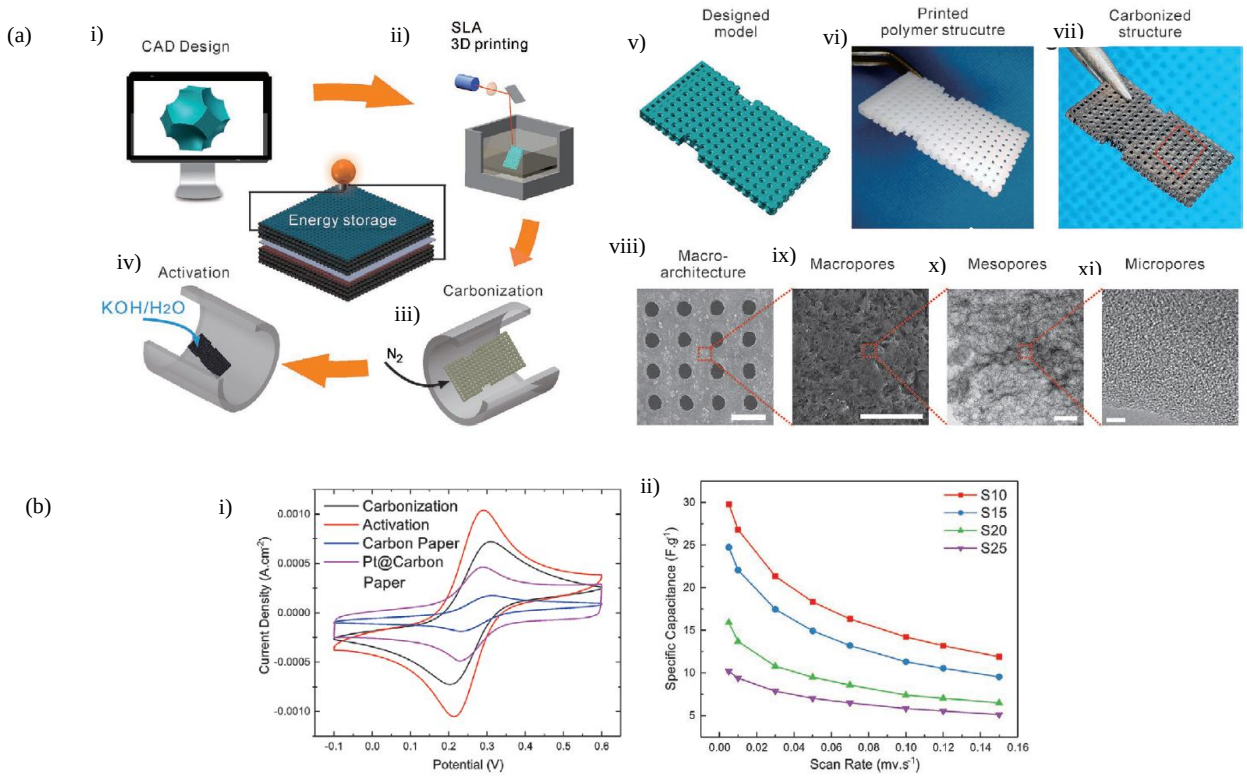

Figure 29. (a) Hybrid process for the preparation of a hierarchical porous electrode: (i) CAD design of the electrode with spherical and cubic pores; (ii) SLA printing; (iii) carbonization; (iv) activation. Pictures of: (v) CAD design of the porous electrode; (vi) printed porous polymer structure; (vii) carbonized electrode. Electron microscopy (SEM and TEM) images of the printed carbon electrode samples: (viii) SEM picture of the macro-architecture after

activation; (ix) SEM picture of the wall surface of the activated electrode; (x, xi) TEM pictures of the activated carbon material; scale bars are 1 mm (viii), 20 µm (ix), 100 nm (x), and 5 nm (xi). (b) Electrochemical results: (i) CV curves (50 mV s^{-1}) of carbonized electrode, with or without steam activation, compared to commercial carbon paper, with or without platinum loading, (ii) Specific capacitance of the electrode with a diameter of 1.0 to 2.5 mm for printed structures used as supercapacitor electrode. Reproduced under terms of the Creative Commons Attribution License from [89]. Copyright 2020, Published by Wiley-VCH.

3D printing followed by pyrolysis has also been exploited at the nanoscale to broaden the field of applications. Thus, Kwon et al. [90] manufactured a nano-micro hierarchical structure with a DLW process (see Supplementary Information) based on TPP for high-performance microsupercapacitors (MSC) electrodes. A photoresin (SU-8) nano-pillar pattern was printed on a silicon dioxide/silicon substrate to form a photoresin interdigitated electrode (PR-IDE) and was then pyrolyzed at 1000 °C. Cyclic voltammetry measurements carried in aqueous Na_2SO_4 electrolyte gave an areal specific capacitance of 193 and 105 µF cm^{-2} at scan rates of 20 and 100 mV s^{-1}, respectively **(Figure 30)**. A capacitance retention of about 95 % for 5000 cycles indicated good stability. These results are comparable to those of other carbon-based MSCs (50-500 µF cm^{-2}). The authors also noted that electrodes with nano-micro pillar structure had a larger areal capacitance than electrodes with micropattern only, confirming their potential for high-power pseudo-capacitor applications.

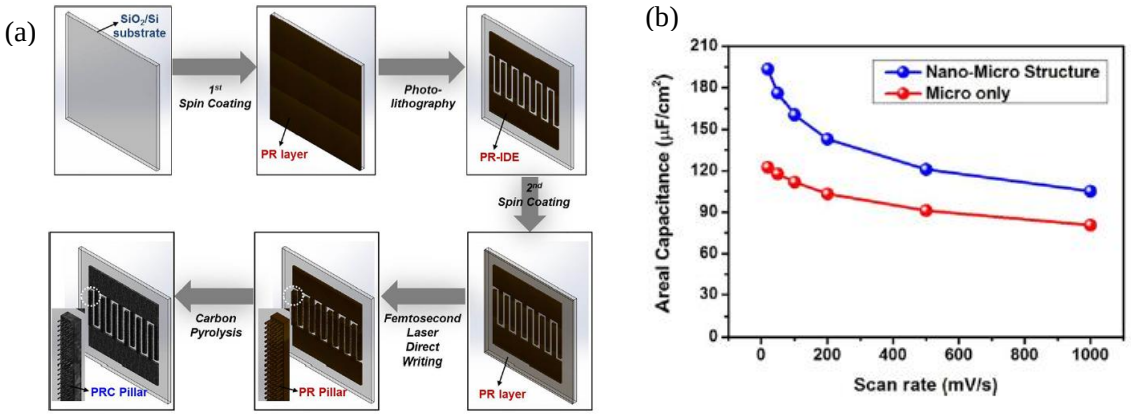

Figure 30. (a) Schematic diagram showing the manufacturing process of a carbonized PR-IDE with a nano-micro hierarchical structure; (b) Specific areal capacitance of the MSCs as a function of scan rate. Reproduced with permission from [90]. Copyright 2018, AIP Publishing.

Yang et al. [91] have developed a new method using TPP followed by pyrolysis for the highly reproducible fabrication of freestanding microelectrodes with a carbon electroactive surface suitable for implantable neurochemical detection. Micro-cones and micro-spheres were printed **(Figure 31a)** with commercial photopolymer (IP-S from Nanoscribe) on a metal anchor wire and pyrolyzed by rapid heat treatment. Glassy carbon-like microelectrodes with diameters of 30 to 70 µm were obtained. The peak-to-peak separation (ΔE_p) of spheres and cones obtained by CV in $Ru(NH_3)_6Cl_3$ were similar (values of 106 and 108 mV, respectively), while the current was twice as high for the cones due to their larger surface area **(Figure 31b)**. These results demonstrated rapid electron transfer at both electrodes, making them suitable for neurochemical detection.

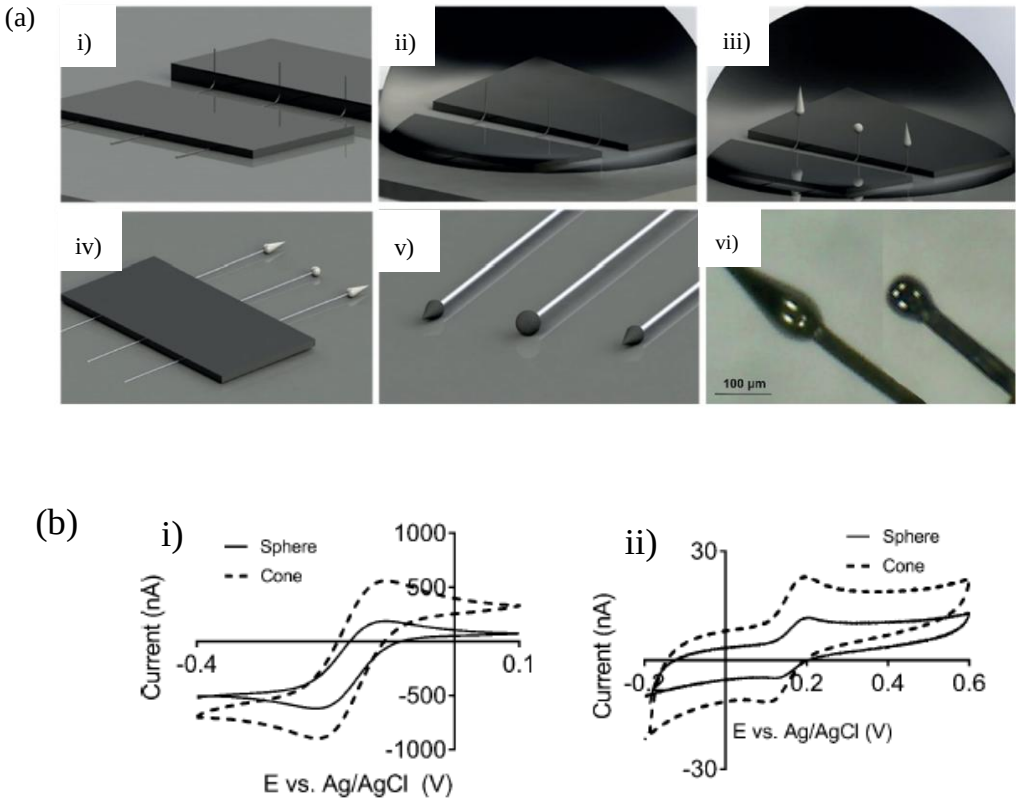

Figure 31. (a) Process for manufacturing 3D-printed carbon electrodes: (i) Freestanding wires are set between two silicon wafers and pointed upwards; (ii) A layer of photoresist is put over the wires; (iii) The electrodes are printed with the laser; (iv) The photoresist is developed, leaving the freestanding electrodes; (v) The electrodes are pyrolyzed; (vi) Optical microscopy image of 3D-printed carbon microelectrodes. (b) Cyclic voltammograms of 3D-printed carbon microelectrodes in: (i) 10 mM $Ru(NH_3)_6Cl_3$, and (ii) 50 µM dopamine. The scan rate was 100 mV s^{-1} . Reproduced with permission from [91]. Copyright 2018, Wiley-VCH.

3D-printed neurotransmitter sensors were also studied by Cao et al. [92] **(Figure 32a)**. The nanostructures were printed by direct laser writing system using a commercial IP-S photoresin, heat-treated in two steps (in oxygen at 450 °C than in argon at 900 °C), insulated by atomic deposition of Al_2O_3, and finally polished into a disc shape by a focused ion beam to produce a 600 nm diameter tip. Due to its small surface area, the electrode showed a typical

background charging current of less than 1 nA **(Figure 32b)**, which is relatively small compared to the hundreds of nano-amps of a typical carbon fiber microelectrode. Similarly, the detection limit for dopamine (proportional to surface area) was measured at 177 nM, which is larger than for the carbon fiber (measured at 20 nM) or the 3D-printed microelectrode (11 nM). However, this limit is acceptable for detecting stimulated dopamine in animal brains, as the nano-electrodes can get closer to release sites (such as synapses) where concentrations are higher. Overall, 3D printing at the nanoscale is a promising strategy for manufacturing electrode sensors as implantable neural devices.

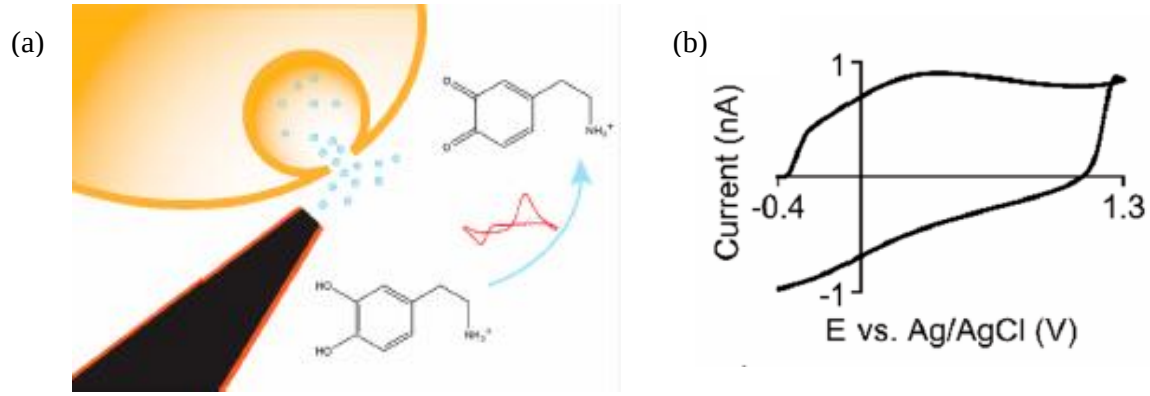

Figure 32. (a) Schematic representation of a carbon nano-electrode in the presence of dopamine; (b) Corresponding background current. Reprinted with permission from [92]. Copyright 2020, American Chemical Society.

3D-printed and then pyrolyzed electrodes showed impressive properties compared to 3D-printed composite electrodes or conventional machined electrodes. Indeed, pyrolysis leads to a higher specific surface area, which increases the number of electrochemically active sites and thus improves their performance. However, control of the structure (architecture and porosity) before and after pyrolysis is essential to fine-tune these carbon electrodes.

In order to bring a more sustainable character to the elaboration of carbonaceous materials, but also for their intrinsic qualities, bio-based precursors (such as lignin, tannins, cellulose,

starch, etc.) are widely represented in recent research. Shao et al. [93] used lignocellulosic materials for the development of 3D-printed monolithic carbon materials with both conductive and structural functionalities. A gel composed of micro fibrillated cellulose (MFC), lignosulfonate (LS), and cellulose powder (CP) was printed using a DIW printer, air-dried, and then heat-treated between 400 and 1200 °C under nitrogen flow **(Figure 33 a)**. The resulting carbons exhibited improved porosity at high heat-treatment temperatures (HTTs) **(Figure 33b)**, which led to a high interfacial area between the electrolyte and the carbon-based electrode. Above 900 °C, MFC/LS/CP carbons not only had a high electrical conductivity of 47.8 S cm^{-1} (1.05 S cm^{-1} at 700 °C) with a porosity of 58 % but also achieved an elastic modulus of 6.62 GPa, higher than that of the precursor, 4.05 GPa. The authors believed that the interesting electrical and mechanical results are promising for the applications of bio-based carbon electrodes.

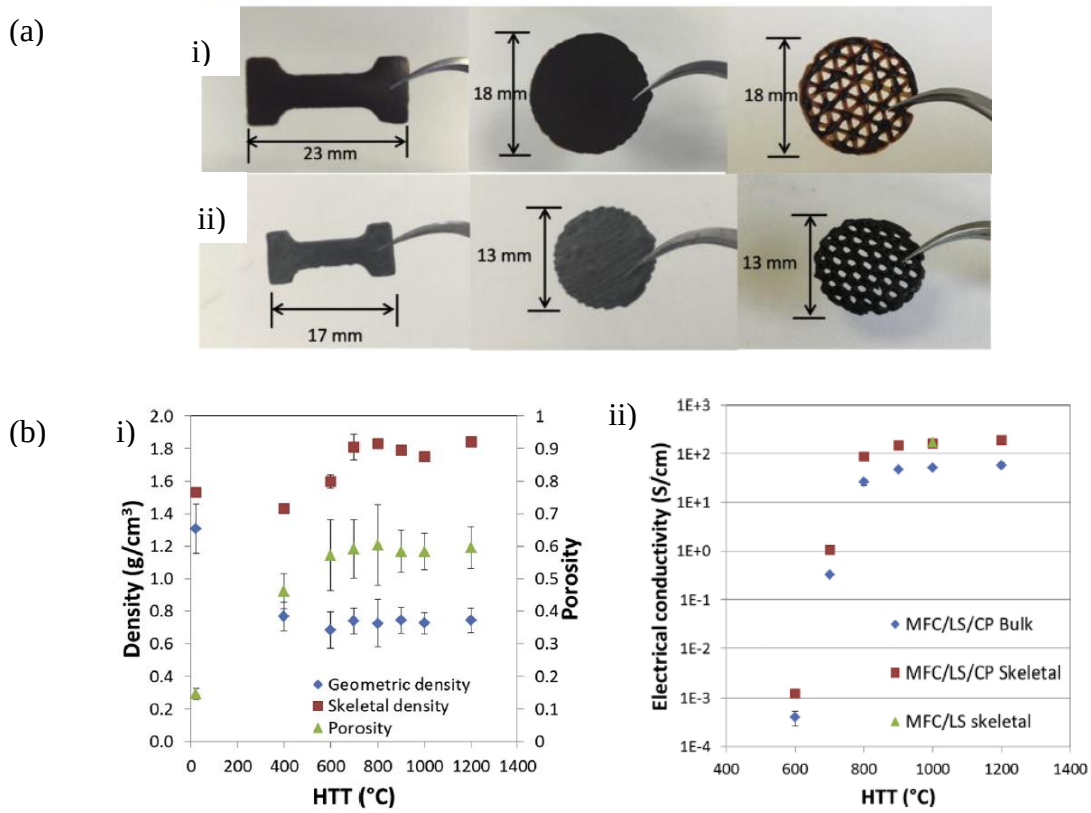

Figure 33. (a) Photographs of: (i) 3D-printed objects from MFC/LS/CP hydrogel after air drying; and (ii) after pyrolysis at 1000 °C; (b) Evolutions of: (i) density and porosity and (ii) bulk and skeletal electrical conductivity of MFC/LS/CP carbon, as a function of the heat-treatment temperature. Reproduced with permission from [93]. Copyright 2018, Elsevier.

Similar carbon precursors have been used by Roman et al. [94] The authors have developed a new approach for the realization of graphene micro-lattices with tunable density from lignin-graphene oxide inks **(Figure 34a)**. Alkali lignin was mixed with GO, in various ratios, to ensure a high carbon yield during carbonization of the more or less dense graphenic structure. Freestanding hollow cylinders were printed by the DIW method, dried, and finally carbonized under argon at 1000 °C. The authors noted that pure GO inks led to a highly compressible aerogel-like carbon structure with measured electrical conductivity equal to 14 S cm^{-1}. The addition of lignin allowed denser structures to be printed (bulk density of 1.69 g cm^{-3} for 30/70 GO/lignin ink compared to 0.2 g cm^{-3} for pure GO ink) with improved

conductivity, with a value of 560.5 S cm^{-1} **(Figure 34b)**. It was shown that the mechanical and electrical properties of graphene micro lattices could be adjusted by playing with density and porosity when changing the GO/lignin ratio.

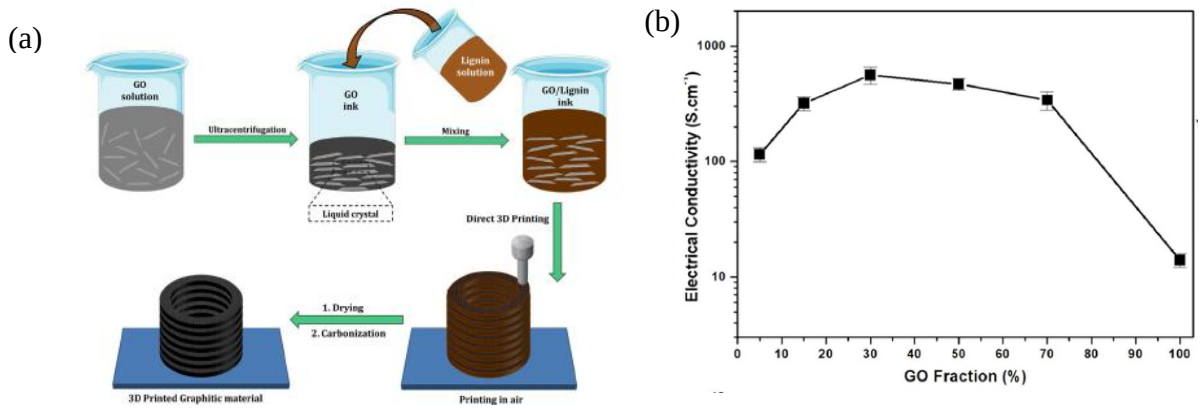

Figure 34. (a) Schematic illustration of the fabrication strategy for 3D printing carbon materials based on lignin-GO inks; (b) Corresponding electrical conductivity as a function of the initial GO fraction. Reprinted with permission from [94]. Copyright 2020, Elsevier.

Recently, Zhou and Liu [34] demonstrated a 3D-printing process for the fabrication of a porous carbon structure with tailorable pore size. Based on the DIW approach, a starch/gelatin ink was prepared as printing feedstock and carbon source, while monodispersed SiO_2 spheres were used as fillers and hard templates. After printing, the materials were freeze-dried and then pyrolyzed at 1100 °C under N_2 atmosphere. The SiO_2 template was removed with NaOH (2 mol L^{-1}) and the remaining alkalis were eliminated by HNO_3 (2 mol L^{-1}) **(Figure 35a)**. The printed carbon had multi-level pores formed by the macro-scale structure, the tailorable meso/macro-porous structure produced by hard templating (related to the size of the silica spheres), and the intrinsic microporosity of the carbon material. The authors evaluated the catalytic performance of the printed carbon material with the selective oxidation of benzyl alcohol in the liquid phase. A printed carbon monolith, prepared with SiO_2 spheres of 200 nm in diameter (PCR-200), with open macroporosity of 63.9 %, led to a conversion of about 90

%. Lower results were obtained with a monolith without hard template (PCR-0), with a conversion of 66 %, or with a monolith with hard template and closed porosity (PCR-200, open porosity 0 %), with a conversion of about 70 %, see **Figure 35b**. The tailored open porous structure increased the contact area between catalyst and reagents, enhancing mass transfer during the reaction. This simple and inexpensive method of fabricating custom-printed porous carbon materials is promising for developments beyond catalysis.

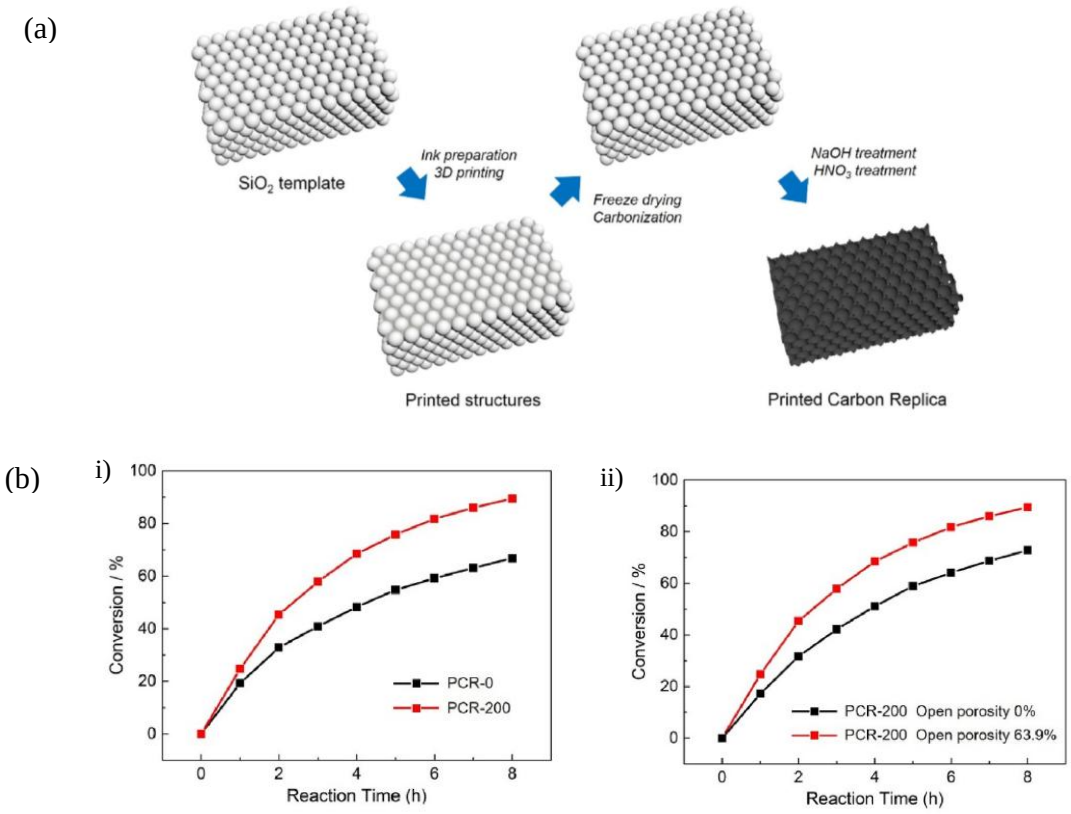

Figure 35. (a) Scheme of the fabrication process of porous carbon replicas; (b) Catalytic performance of the resulting printed carbon monoliths: conversion and selectivity of benzyl alcohol on monoliths: (i) with different porous structures, or (ii) with different open porosities. Reprinted with permission from [34]. Copyright 2020, Elsevier.

The multi-stage printing of carbon materials remains a promising way to obtain highly functional customized materials, suitable for multiple applications such as electrochemistry due to their porosity and electrical conductivity. However, the porosity is often generated in

an uncontrolled manner during pyrolysis. Controlling porosity in such carbon structures thus remains a major challenge.

4.2 Direct printing of carbon

Direct printing of carbon can be difficult and is, to date, less represented in publications. As mentioned above, additive manufacturing is not directly applicable to carbon, so obtaining carbon materials generally requires a multi-step process including pyrolysis. However, it is still possible to obtain 3D-printed carbon structures without a pyrolysis step. We propose here to differentiate two categories: the printing of carbon on a support by means of an ink on the one hand, and the in-situ synthesis of carbon during the 3D printing process on the other hand. To date, the main method applied to obtain this type of carbon structure is ink-printing (inkjet or direct ink writing).

4.2.1 Printing by ink intermediary

Recently, Llinas et al. [95] studied origami terahertz (THz) detectors made by inkjet printing of aqueous inks based on carbon nanotubes. The printed structure was just dried in vacuum and did not require a pyrolysis step. The aim was to obtain high-performance THz detectors at room temperature, i.e., to achieve the lowest noise-equivalent power (NEP = noise/signal). Ultra-flexible p-type, n-type, and p-n junction CNT films were obtained after printing and water removal **(Figure 36)**. The photo-thermoelectric response of devices with channels of varying widths and lengths was investigated using a 532 nm focused laser. A NEP of 42 nW $Hz^{-1/2}$ was obtained on a 110 µm-thick PET plate for p-n junction when an improved NEP value of 31 nW $Hz^{-1/2}$ was obtained on a 0.9 µm-thick PET substrate. The authors were able to extend this approach to a six-junction origami detector and obtained a NEP of 12 nW $Hz^{-1/2}$, approaching some of the best THz detectors based on CNTs.

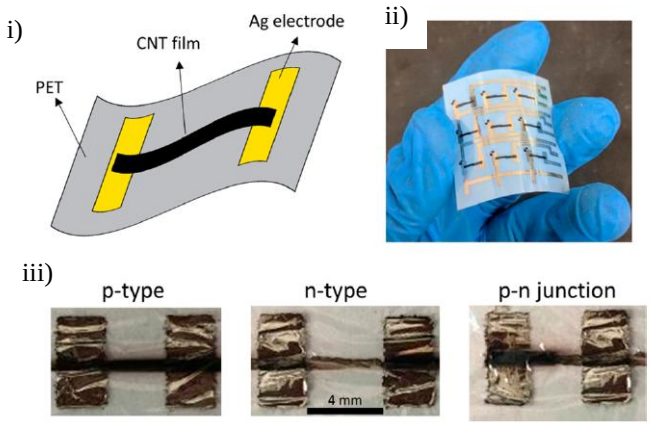

Figure 36. Inkjet printing of THz photodetectors: (i) illustration of the PET substrate onto which Ag electrodes and CNT films are inkjet-printed, (ii) optical image of an array of CNT-based devices printed on a 110 µm-thick PET plate, (iii) optical image of CNT-based devices printed on a 0.9 µm-thick PET plate. Reprinted with permission from [95]. Copyright 2020, American Chemical Society.

The approach of printing carbon materials without a pyrolysis step has been applied to energy storage devices to operate miniaturized electronics, and 3D-printed supercapacitors are a good example of this. Chen et al. [96] reported the use of the DIW technology for printing fully packaged flexible supercapacitors composed of a SWCNTs electrode and a PVA-based gel electrolyte **(Figure 37a)**. The electrodes were printed (and directly dried using the heated build platform) with a water-based CNT ink in the presence of surfactants, and then treated under acidic conditions to remove the sodium from the surfactants, which improved the electrical conductivity of the CNT electrode. The PVA-based electrolyte was subsequently printed on top of the electrodes. The authors studied the impact of the electrode and electrolyte design (gap distance between two electrodes and width of the electrode pattern) on the supercapacitor performance. The electrochemical study showed that a smaller gap distance between two electrodes and wider electrodes enhanced the capacitance of the as-printed supercapacitor. Indeed, the specific capacitance decreased from 13.37 F cm^{-3} to 3.88 F

cm^{-3} as the gap distance increased from 0.1 to 0.4 cm, while it increased from 7.15 F cm^{-3} to 15.34 F cm^{-3} when increasing the electrode width from 0.2 to 0.25 cm, see **Figure 37b**).

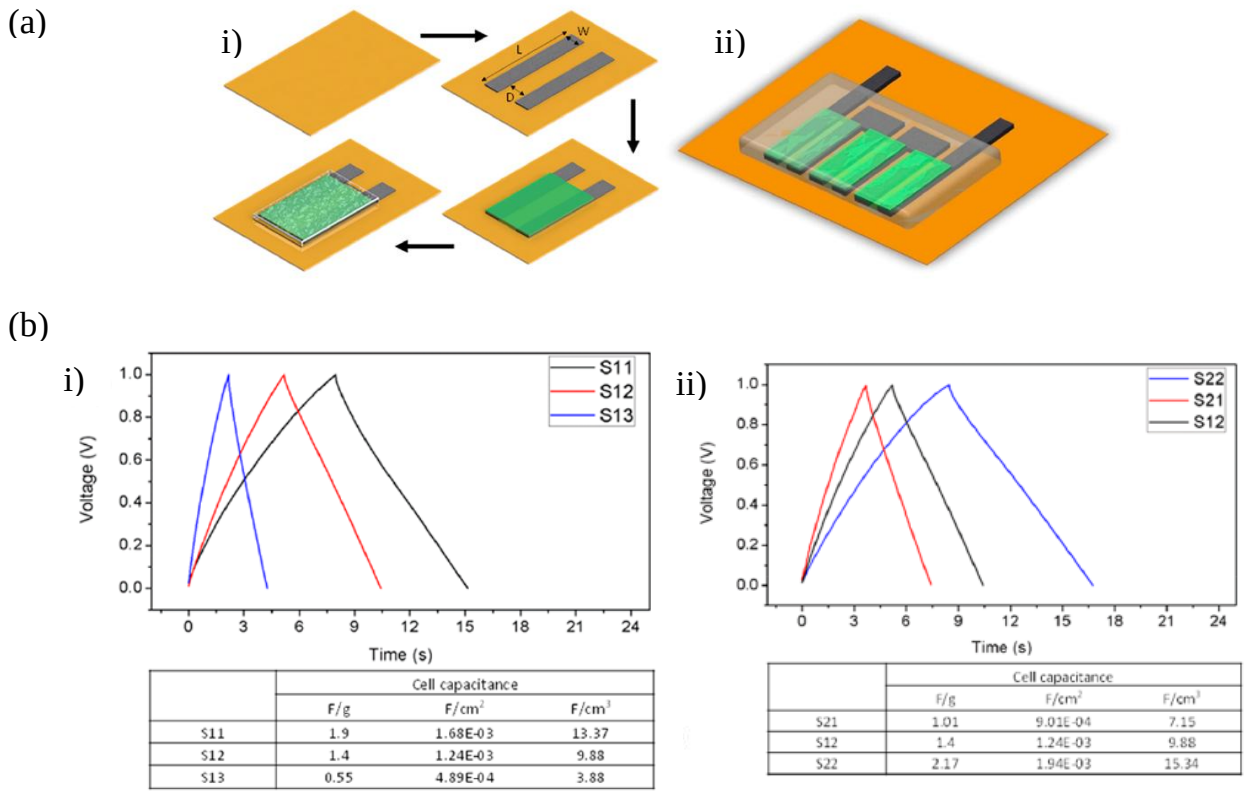

Figure 37. (a) i) Scheme of the layer design and DIW printing process of supercapacitors, and ii) array of three identical cells connected in series; (b) Galvanostatic charge/discharge curves at 1.32 A cm^{-3} for cells with: i) different electrode gap distances (S11 = 0.1 cm; S12 = 0.2 cm and S13 = 0.4 cm), and ii) different electrode widths (S21 = 0.15 cm; S12 = 0.2 cm and S22 = 0.25 cm). Reprinted in parts with permission from [96]. Copyright 2017, American Chemical Society.

In the same year, Yu et al. [97] proposed a versatile 3D printing technique for fabricating CNTs-based micro-supercapacitors (MSCs). The printing ink was prepared by milling a moderate amount of CNTs in a solution of IPA, ethylene glycol, and a dispersing agent. The electrodes were printed on a heated base to facilitate evaporation of the solvent and adhesion between the printed layers, thereby improving the structural integrity of the structure **(Figure**

38a). The areal capacitance of the MSC was calculated to be 0.732 mF cm-² at a scan rate of 100 mV s^{-1}. After heat treatment at 350 °C to remove the dispersing agent, the areal capacitance increased to 4.25 mF cm^{-2} (larger increases were found at a scan rate of 50 mV s^{-1} and for galvanostatic charge-discharge measurements).

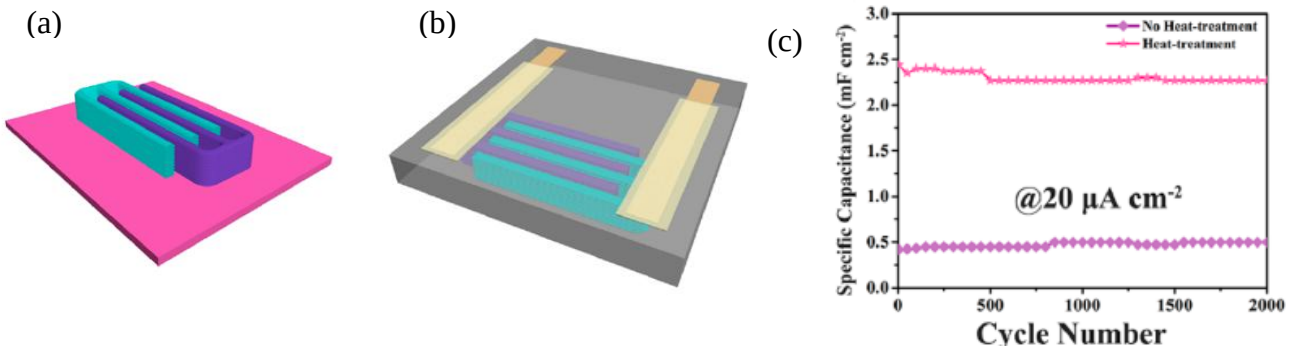

Figure 38. (a) Schematic illustration of 3D-printed interdigitated electrodes; (b) Packaged MSCs; (c) Specific capacitance of heat-treated and non-heat-treated 6-layer packed MSCs; Reprinted with permission from [97]. Copyright 2017, American Chemical Society.

However, the printing accuracy strongly depends on the ink viscosity and used particles. Jiang et al. [98] demonstrated a promising technique as a general strategy for graphene-based aerogels: an ion-induced gelation method for fabricating graphene-based aerogel micro lattices with structures produced by DIW. GO inks were prepared by adding traces of $CaCl_2$ as cross-linker in an aqueous GO solution **(Figure 39)**. After printing, freeze-drying and chemical reduction of GO were carried out. The 3D-printed GO aerogels exhibited a compressive stress value at 80 % strain of about 90 kPa and an electrical conductivity of about 800 S m^{-1} at a density of 10 mg cm^{-3}, which exceeded most conventional graphene aerogels. This technique was also suitable for GO/CNT inks for which the electrical conductivity increased (up to about 1000 S m^{-1}), providing excellent capacitive performance for supercapacitors. This printing technique is promising for a wide range of applications.

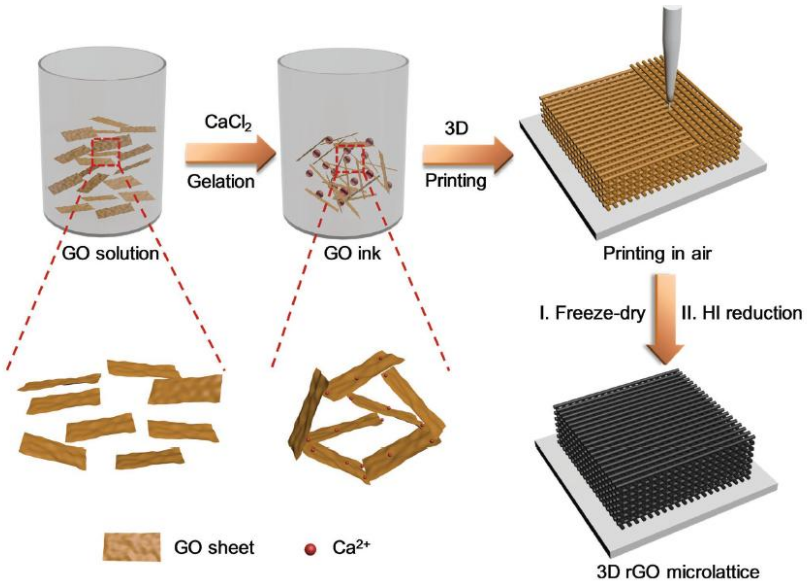

Figure 39. Schematic illustration of the 3D-printing process of rGO microlattice: a trace amount of $CaCl_2$ is added to a GO solution to form a GO ink with favorable rheological properties. The GO gel ink is then extruded through a robot-assisted nozzle to build a 3D architecture. Next, the micro lattice is freeze-dried to obtain a rigid GO aerogel and further reduced by HI (55 % in ethanol/water solution) to obtain a printed graphene aerogel microlattice. Reproduced with permission from [98]. Copyright 2018, Wiley-VCH.

Wishing to highlight the possible sustainability aspect of supercapacitor electrode materials, Idrees et al. [99] proposed to use porous carbon derived from packaging waste to print a supercapacitor in 3D. Activated carbon was prepared from the carbonization of loose-fill packaging and its activation with NaOH, and was then added to an electrolytic solution. The activated carbon paste (content of carbon about 35 wt.%) was then extruded to form electrodes **(Figure 40a)**. The device developed had a capacitance of 328.95 mF cm^{-2} at 2.5 mA (decreasing with the current, see **Figure 40b**), the highest among all-solid-state supercapacitors made by extrusion-based 3D-printing (maximum carbon content of 35 wt.% compared to 2-11 wt.% for other carbon- or graphene-based extruded parts), but was still

limited by the rheology of the ink, which is a crucial factor for the extrusion-printing technique.

(a)

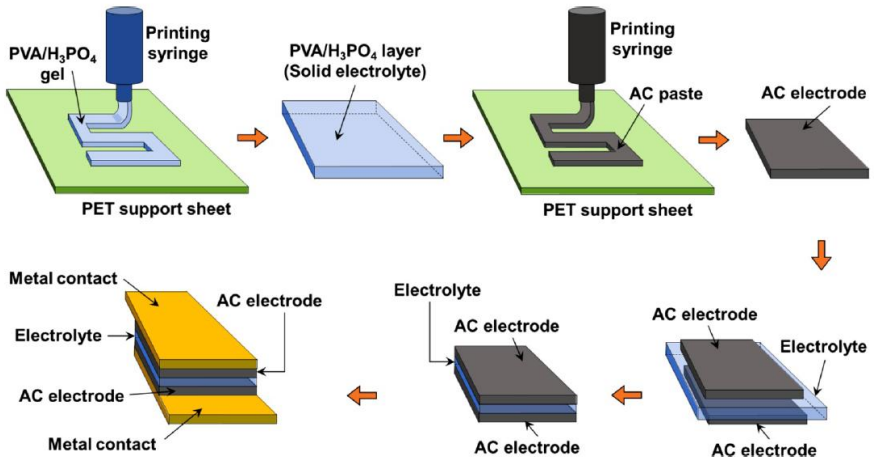

(b)

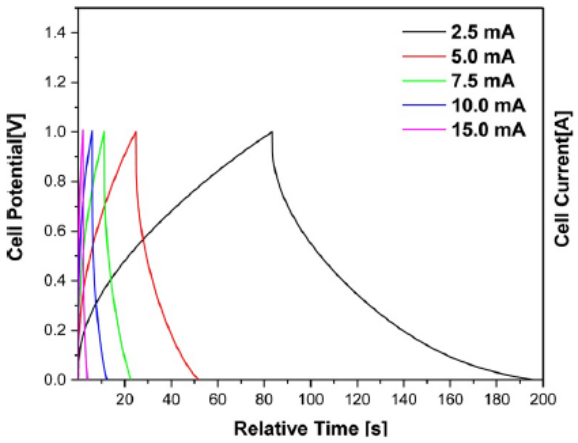

Figure 40. (a) Schematic representation of the supercapacitor fabrication process; (b) Galvanostatic charge/discharge curves at various applied currents. Reprinted with permission from [99]. Copyright 2020, Elsevier.

Besides supercapacitors, directly printed porous carbon materials are widely used and developed for battery electrodes. Lacey et al. [100] have worked on advanced battery electrodes with hierarchical porosity printed from an aqueous ink with a high content of holey graphene oxide (hGO). After extrusion, freeze-drying (used to remove the remaining H_2O), and thermal reduction at 1000 °C in argon, the discharge performances at 0.1 mA cm^{-2} current density were tested. The reduced 3D-printed meshes (r-hGO) were able to provide a

remarkable areal capacity of 13.3 mA h cm^{-2}, whereas the same materials prepared as a vacuum film provided only an areal capacity of 0.21 mA h cm^{-2} **(Figure 41a)**. The authors noted that the 3D-printed hGO mesh exhibited multiple levels of porosity **(Figure 41b)**, which facilitates the accessibility of active sites in the structure as well as ion transport, thereby improving the performance of Li-O_2 batteries.

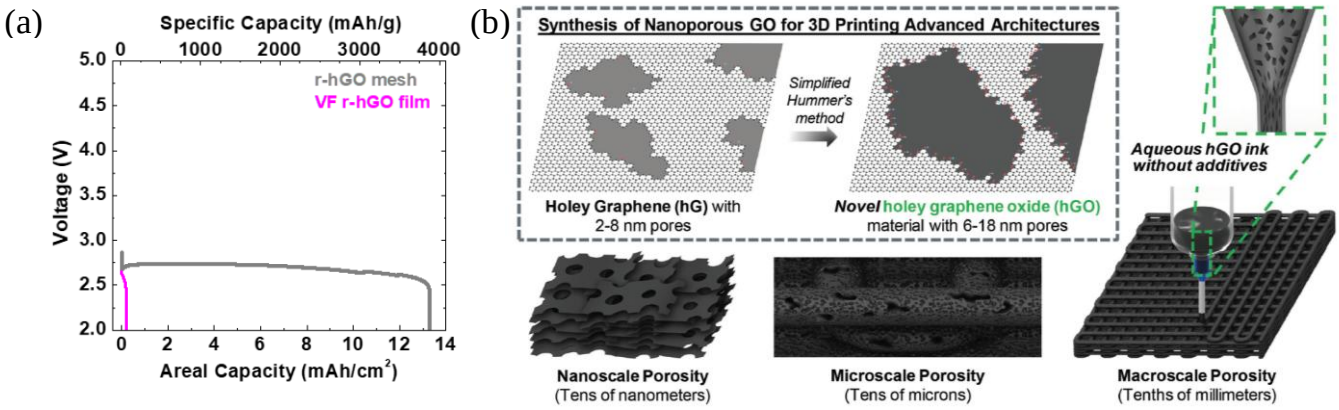

Figure 41. (a) Full discharge performance of vacuum film r-hGO and r-hGO 3D-printed mesh at 0.1 mA cm^{-2}; (b) Schematic representation of the processes used to synthesize hGO, a highly porous 2D nanomaterial, and to create an aqueous, additive-free printable hGO ink for the extrusion of complex 3D architectures with hierarchical porosity (from macro to nanoscale). Reproduced with permission from [100]. Copyright 2018, Wiley-VCH.

At the same time, Qiao et al. [101] studied 3D-printed GO structures for Li-CO_2 batteries. rGO meshes were printed in the same way as Lacey et al. [100], thermally reduced at 300 °C, and were then immersed in an aqueous $NiCl_2$ solution (0.05 mol $L^{-1)}$. Finally, the Ni nanoparticles were anchored on the structure through rapid (54 ms) and high-temperature (1627 °C) thermal shock. Such Ni/rGO structure as a cathode in a Li-CO_2 battery was able to provide a high areal capacity of 14.6 mA h cm^{-2}.

The need for high resolution is a recurring theme in all 3D-printing techniques and especially for electronic components or supercapacitors as presented above. Goh et al. [102]

were able to obtain high-resolution conductive paths with carbon nanotubes printed in twin-lines using the aerosol jet printing technique (AJP) based on evaporation-driven self-assembly of CNTs. Details on the AJP technique are available in the Supplementary Information. Depending on the printing speed, narrow lines with a width between 30 and 80 µm were obtained. The preferential alignment of CNTs along the edges of the printed lines during the evaporation of the water in the ink (evaporation-induced self-assembly, also known as "coffee-ring effect", see **Figure 42a**) led to conductive tracks 600-1500 nm wide on each side of the deposited lines **(Figure 42b)**. The high resolution achieved by the AJP process means that this printing technique has the potential for the fabrication of CNT-based high-speed electronic devices.

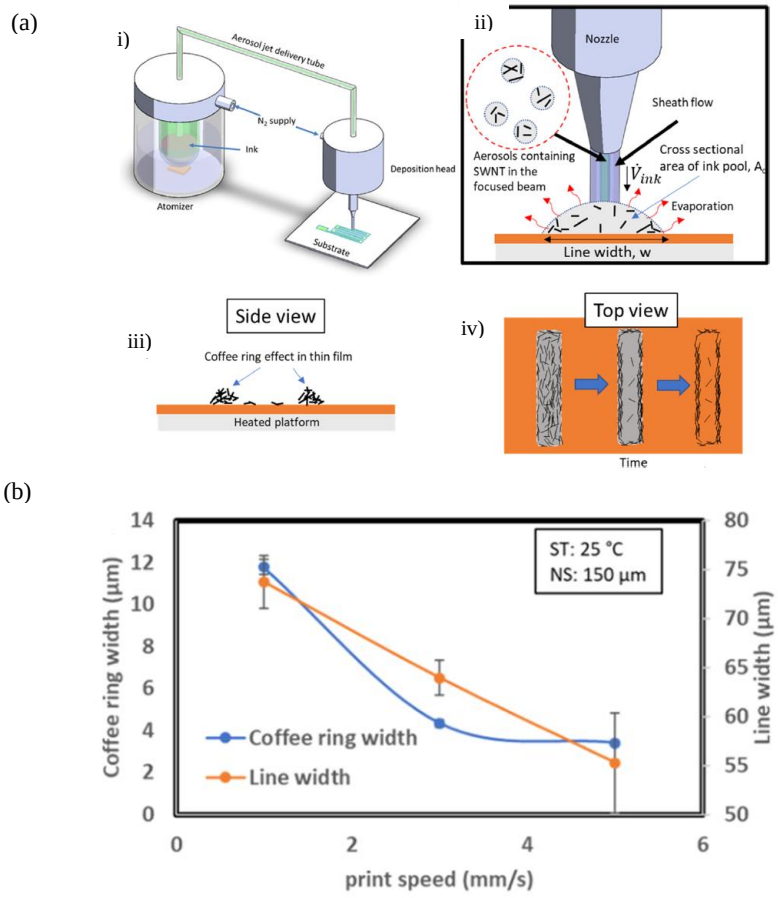

Figure 42. (a) i) Scheme of the aerosol jet printing process (atomization, aerosol transportation and ink deposition), ii) zoom on the aerosol jet deposition from the nozzle and

the evaporation process on the substrate, iii) and iv) schemes depicting the preferential alignment of CNT, known as coffee-ring effect ; (b) Measurement of the twin-lines width and conductive tracks width (coffee-ring width), and effect of the print speed. Reprinted with permission from [102]. Copyright 2019, American Chemical Society.

Recently, Lu et al. [103] demonstrated an AJP process that resulted in high uniformity and increased printing stability for CNT-based, thin-film transistors through precise control of the temperature of the CNT ink bath **(Figure 43a)**. Reducing the ink bath temperature from 32 to 8 °C improved ink atomization **(Figure 43b)**, resulting in an increase in film density and hole mobility of 12.5 $cm^2\ V^{-1}\ s^{-1}$, but also improved uniformity and printing stability.

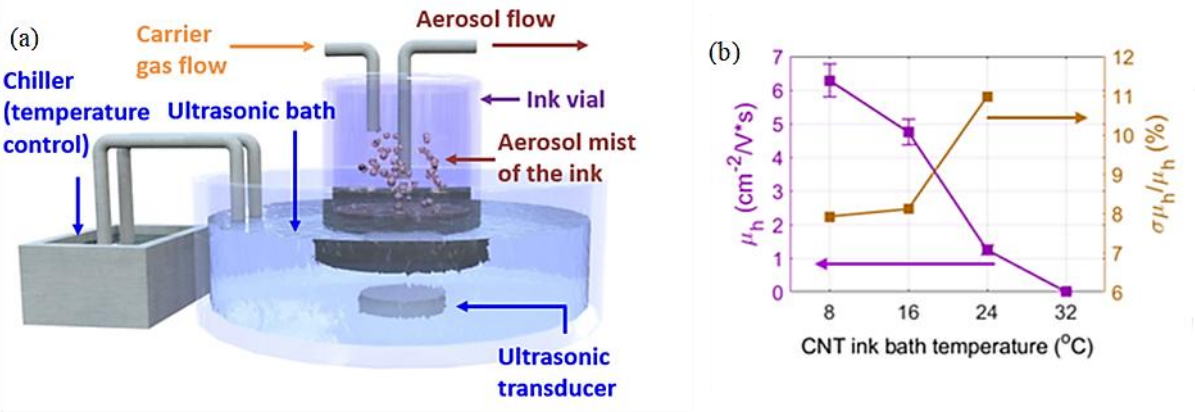

Figure 43. (a) Ultrasonic atomizer for the aerosol jet printer (connected to a chiller to control the temperature of the bath and thus of the ink) used to print thin films based on CNTs; (b) Hole mobility (μ_h, left axis) and relative variation of the hole mobility ($\sigma(\mu_h)/\mu_h$) as a function of the temperature of the CNT ink bath. Reprinted in parts with permission from [103]. Copyright 2020, American Chemical Society.

The high-resolution AJP technique has also been successfully applied in the field of biology. Indeed, Parate et al. [104] developed an aerosol jet-printed graphene immunosensor for label-free cytokine in bovine serum **(Figure 44a)**. The interdigitated electrodes (IDEs), composed of 50 microstrips of 40 µm-wide deposited graphene lines, have demonstrated high

electrical conductivity (about 10^4 S m^{-1}) at low thickness (about 25 nm). The upper surface of the graphene electrode was functionalized with oxygen-containing groups (by annealing in a CO_2 environment) to improve its electroattractive response. The graphene biosensor functionalized with interferon-gamma (IFN-γ) and interleukin-10 (IL-10) bovine antibodies showed a highly selective response time with low detection limits **(Figure 44b)**. This readily functionalized graphene biosensor is therefore well suited for rapid sensor applications, such as bacteria sensing, ion, and protein monitoring, or strain sensing.

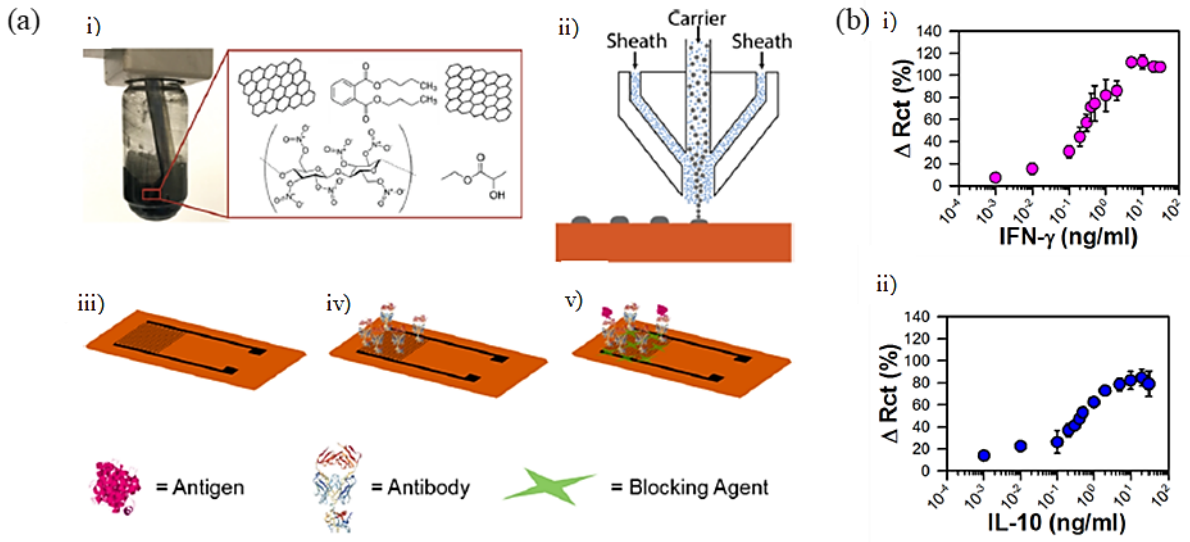

Figure 44. (a) Schematic representation of the fabrication by AJP and biofunctionalization of graphene IDEs: (i) formulation of the graphene ink for aerosol printing, (ii) AJP mechanism of the graphene ink showing a sheath gas enveloping the carrier stream of aerosolized graphene ink particles to focus the ink to a desired diameter, (iii) graphene IDEs on a polyimide sheet, (iv) antibodies selective to IL-10 or IFN-γ immobilized on the graphene surface functionalized by carboxyl groups, (v) the remaining exposed surface of the graphene sensor is covered with the blocking agent (mixture of bovine serum albumin, fish gelatin, and Tween-20) and incubated with antigen; (b) Percentage change in charge transfer resistance

relative to the change in concentration of i) IFN- γ and ii) IL-10. Reprinted with permission from [104]. Copyright 2020, American Chemical Society.

The use of an ink has thus enabled the production of high-resolution carbon structures, leading to excellent responses to various stimuli. Indeed, 3D-printing techniques that use an ink allow for a high carbon loading in the final device composition. However, the prerequisites and specifications of each technique can moderate the implementation of these materials with high carbon content.

Direct 3D printing of full-carbon objects with a binder-free system remains a challenge. Laser-assisted in-situ carbon synthesis during the printing process (see below) can thus be seen as an interesting and complementary alternative for the fabrication of 3D full-carbon objects.

4.2.2 In-situ synthesis of carbon

Sha et al. [37] studied the in-situ synthesis of freestanding 3D graphene foams (GFs) using the SLS technique with a CO_2 laser to convert a Ni/sucrose mixture **(Figure 45)**. The 3D-printed foams contained high-quality few-layer graphene, had a high porosity of about 99.3 %, and a low density of about 0.015 g cm^{-3}. They also had a remarkable storage modulus of about 11 kPa and a high damping capacity of about 0.06 at room temperature, values comparable to GFs prepared by powder metallurgy templates and other methods. This simple and efficient method has given promising results that can be used to form macroscopic monoliths of various shapes for many applications.

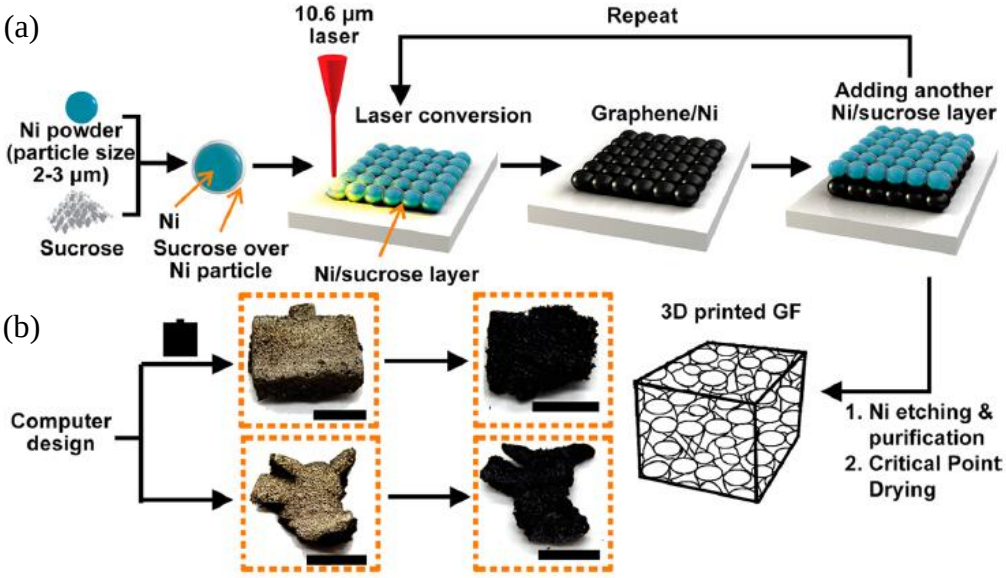

Figure 45. (a) Scheme of the in-situ synthesis of 3D GFs; (b) Photographs of 3D-printed GFs before and after dissolution of Ni. Scale bars are 5 mm. Reprinted under ACS Author Choice Open access terms from [37]. Copyright 2017.

More recently, Luo et al. [36] reported on a direct laser writing-assisted method for producing porous carbon platelets (PCP) with tailored shape and porous structure. Electrically conductive carbon patterns were formed by CO_2 laser irradiation of a carbonizable substrate made of cellulose paper and sodium lignosulfonate. Limited by the laser processing equipment, the authors were still able to produce a disc with a diameter of 490 μm and a thickness between 35 and 53 μm **(Figure 46)**. The applications of such highly porous, versatile porous carbon platelets as dye adsorbent, flexible sensor, and miniaturized supercapacitor were also demonstrated and might be developed further in the future.

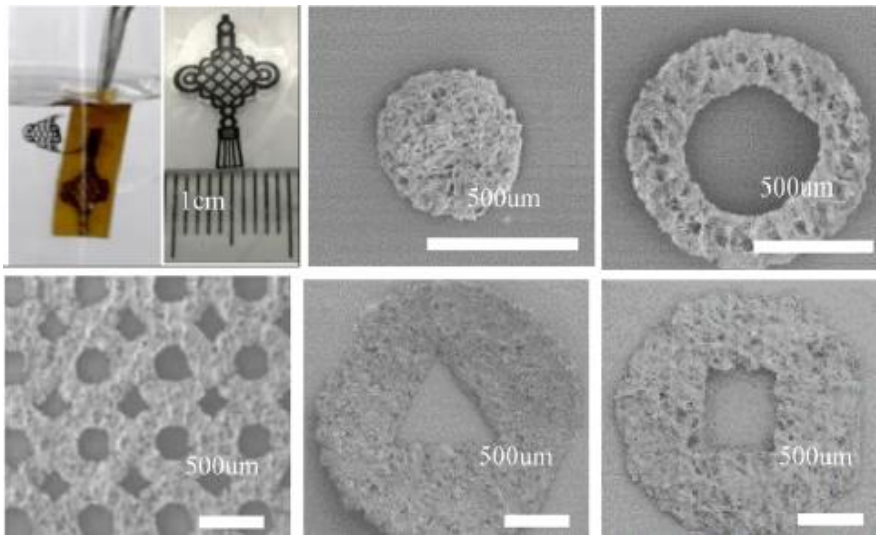

Figure 46. SEM micrographs of PCPs with various geometric patterns predesigned by a CAD program; Reprinted under ACS Author Choice Open access terms from [36]. Copyright 2019.

5. Conclusion

In this paper, we have reviewed the main recent developments in carbonaceous materials in 3D printing. We discussed in detail the types of materials, fabrication and performance of printed carbon-based structures.

While 3D printing of carbon composites can be seen as a well-understood process for enhancing the mechanical properties of polymer matrices or taking advantage of certain properties of carbon (e.g., electrical conductivity, microwave absorption), the advances in 3D printing of pure carbon materials have been impressive. However, as an emerging technology, many challenges remain.

Obtaining 3D carbon material through a multi-step process is promising. Easily applicable over a wide range of resolution (from nanometers with TPP to micrometers with other methods), this process, however, usually requires a long preparation to obtain a final carbon structure: printing, freezing and freeze-drying for gels, or coating in the case of a sacrificial

polymer structure and subsequent pyrolysis. Extensive research has been carried out into the inclusion of bio-based carbon precursors in the matrix formulation to limit petrochemical ingredients as part of a more sustainable approach.

The development and optimisation of new precursors with sufficient carbon yield and low shrinkage would better exploit the advantages offered by 3D printing as a first step in tailoring the architecture and micro-texture of new carbon materials. A better understanding of performance-structure relationships and a focus on controlling the printed architecture on the one hand, and the porosity during pyrolysis through hard templates and/or porogens or other additives on the other hand, will be needed in the future as this is the key to truly governing the final properties of the carbons produced in this way.

In order to reduce the number of processing steps, directly written materials (through direct ink writing, ink jetting and aerosol jet printing) have been studied and benefited from state-of-the-art production technology with fast drying inks that require little post-printing process and no pyrolysis. However, they suffer from the typical problems of ink/gel printing, as good printability and rheology are often not compatible with a high carbon content and are therefore mainly used in miniaturized electronics.

Nevertheless, the main challenge facing 3D carbon printing is the difficulty of obtaining carbon structures in situ without a binder. Thanks to the development of the high-energy CO_2 laser, pyrolysis can take place at the same time as the printing process, allowing a carbon structure to be obtained in a single step. However, this method is still limited to carbonizable substrates, and the diameter of the laser reduces the printing resolution. This highlights the obstacles to obtaining a tailored carbon structure in situ.

In terms of the typical dimensions of objects that can be produced by additive manufacturing, it is technically possible, using a suitable technique, to 3D print large objects,

such as a house or a bridge. When it comes to the 3D printing of carbon materials, researchers are mainly focusing on micro- and nanoscales where 3D printing can enrich the field. The current trend does not seem to be towards the production of large objects, which can only be achieved by methods using inks rich in carbon particles. Indeed, techniques that require a pyrolysis step could certainly produce objects as large as desired, but their conversion into carbon would then require furnaces whose dimensions, necessarily limited, would then be restrictive. Nor is it certain that pyrolysis of large objects produced layer by layer can yield carbon blocks of sufficient quality in terms of the absence of cracks or other types of defects. So 3D carbon printing definitely seems to be more focused on small devices than on large ones, but perhaps the future will prove us wrong as the technology advances.

Additive manufacturing (AM) has stimulated both academic research and industrial production. However, as a recent process when applied to carbon materials, 3D printing needs to be optimized in terms of understanding the process and material properties. As the printing process is governed by a multitude of parameters, multiphysical modelling of key parameters would definitely accelerate the development of 3D printing with reliable modelling prediction and optimization of the performances of parts produced by AM.

Thus, it is safe to say that 3D printing technologies applied to carbon materials are extremely promising and will remain a hot topic in the future.

Conflict of interests

The authors declare no conflict of interest.

Acknowledgements

PB wishes to thank the French Ministry of Higher Education and Research and by the Grand-Est Region for funding her doctoral fellowship. All authors gratefully acknowledge the financial support of ERDF [TALiSMAN project (2019-000214)].

References

[1] ISO/ASTM, Terminology for Additive Manufacturing - General Principles - Terminology, ASTM International, 2016. https://doi.org/10.1520/ISOASTM52900-15.

[2] T. Campbell, C. Williams, O. Ivanova, B. Garrett, Could 3D printing change the world?, Atlantic council, Washington, 2011.

[3] C.W. Hull, Apparatus for production of three-dimensional objects by stereolithography, US4575330A, 1986. https://patents.google.com/patent/US4575330A/en (accessed July 3, 2020).

[4] J.-C. André, A. Le Mehaute, O. De Witte, Dispositif pour réaliser un modèle de pièce industrielle, FR8411241, 1984.

[5] D.R. Smalley, C.W. Hull, Method of making a three dimensional object by stereolithography, US5130064A, 1992. https://patents.google.com/patent/US5130064/en (accessed July 3, 2020).

[6] T.D. Ngo, A. Kashani, G. Imbalzano, K.T.Q. Nguyen, D. Hui, Additive manufacturing (3D printing): A review of materials, methods, applications and challenges, Composites Part B: Engineering. 143 (2018) 172–196. https://doi.org/10.1016/j.compositesb.2018.02.012.

[7] T. Singh, S. Kumar, S. Sehgal, 3D printing of engineering materials: A state of the art review, Materials Today: Proceedings. 28 (2020) 1927–1931. https://doi.org/10.1016/j.matpr.2020.05.334.

[8] K. Tappa, U. Jammalamadaka, Novel Biomaterials Used in Medical 3D Printing Techniques, JFB. 9 (2018) 17. https://doi.org/10.3390/jfb9010017.

[9] M. Hassan, K. Dave, R. Chandrawati, F. Dehghani, V.G. Gomes, 3D printing of biopolymer nanocomposites for tissue engineering: Nanomaterials, processing and structure-function relation, European Polymer Journal. 121 (2019) 109340. https://doi.org/10.1016/j.eurpolymj.2019.109340.

[10] X. Wang, M. Jiang, Z. Zhou, J. Gou, D. Hui, 3D printing of polymer matrix composites: A review and prospective, Composites Part B: Engineering. 110 (2017) 442–458. https://doi.org/10.1016/j.compositesb.2016.11.034.

[11] H. Wu, W.P. Fahy, S. Kim, H. Kim, N. Zhao, L. Pilato, A. Kafi, S. Bateman, J.H. Koo, Recent developments in polymers/polymer nanocomposites for additive manufacturing, Progress in Materials Science. 111 (2020) 100638. https://doi.org/10.1016/j.pmatsci.2020.100638.

[12] L. Zhou, J. Fu, Y. He, A Review of 3D Printing Technologies for Soft Polymer Materials, Adv. Funct. Mater. 30 (2020) 2000187. https://doi.org/10.1002/adfm.202000187.

[13] Z. Chen, Z. Li, J. Li, C. Liu, C. Lao, Y. Fu, C. Liu, Y. Li, P. Wang, Y. He, 3D printing of ceramics: A review, Journal of the European Ceramic Society. 39 (2019) 661–687. https://doi.org/10.1016/j.jeurceramsoc.2018.11.013.

[14] F. Kotz, K. Arnold, W. Bauer, D. Schild, N. Keller, K. Sachsenheimer, T.M. Nargang, C. Richter, D. Helmer, B.E. Rapp, Three-dimensional printing of transparent fused silica glass, Nature. 544 (2017) 337–339. https://doi.org/10.1038/nature22061.

[15] D. Zhang, X. Liu, J. Qiu, 3D printing of glass by additive manufacturing techniques: a review, Front. Optoelectron. (2020). https://doi.org/10.1007/s12200-020-1009-z.

[16] S. Das, D.L. Bourell, S.S. Babu, Metallic materials for 3D printing, MRS Bull. 41 (2016) 729–741. https://doi.org/10.1557/mrs.2016.217.

[17] H. Nulwala, A. Mirjafari, X. Zhou, Ionic liquids and poly(ionic liquid)s for 3D printing – A focused mini-review, European Polymer Journal. 108 (2018) 390–398. https://doi.org/10.1016/j.eurpolymj.2018.09.023.

[18] S. Mantihal, R. Kobun, B.-B. Lee, 3D food printing of as the new way of preparing food: A review, International Journal of Gastronomy and Food Science. 22 (2020) 100260. https://doi.org/10.1016/j.ijgfs.2020.100260.

[19] A. Al Rashid, S.A. Khan, S. G. Al-Ghamdi, M. Koç, Additive manufacturing: Technology, applications, markets, and opportunities for the built environment, Automation in Construction. 118 (2020) 103268. https://doi.org/10.1016/j.autcon.2020.103268.

[20] S.C. Joshi, A.A. Sheikh, 3D printing in aerospace and its long-term sustainability, Virtual and Physical Prototyping. 10 (2015) 175–185. https://doi.org/10.1080/17452759.2015.1111519.

[21] X. Zhou, C. Liu, Three-dimensional Printing for Catalytic Applications: Current Status and Perspectives, Adv. Funct. Mater. 27 (2017) 1701134. https://doi.org/10.1002/adfm.201701134.

[22] S. Beg, W.H. Almalki, A. Malik, M. Farhan, M. Aatif, Z. Rahman, N.K. Alruwaili, M. Alrobaian, M. Tarique, M. Rahman, 3D printing for drug delivery and biomedical applications, Drug Discovery Today. 25 (2020) 1668–1681. https://doi.org/10.1016/j.drudis.2020.07.007.

[23] D. Douroumis, 3D Printing of Pharmaceutical and Medical Applications: a New Era, Pharm Res. 36 (2019) 42, s11095-019-2575–x. https://doi.org/10.1007/s11095-019-2575-x.

[24] M. Irfan Ul Haq, S. Khuroo, A. Raina, S. Khajuria, M. Javaid, M. Farhan Ul Haq, A. Haleem, 3D printing for development of medical equipment amidst coronavirus (COVID-19) pandemic—review and advancements, Res. Biomed. Eng. (2020). https://doi.org/10.1007/s42600-020-00098-0.

[25] N. Samiei, Recent trends on applications of 3D printing technology on the design and manufacture of pharmaceutical oral formulation: a mini review, Beni-Suef Univ J Basic Appl Sci. 9 (2020) 1–12. https://doi.org/10.1186/s43088-020-00040-4.

[26] K. Fu, Y. Yao, J. Dai, L. Hu, Progress in 3D Printing of Carbon Materials for Energy-Related Applications, Adv. Mater. 29 (2017) 1603486. https://doi.org/10.1002/adma.201603486.

[27] J.P. Mensing, T. Lomas, A. Tuantranont, 2D and 3D printing for graphene based supercapacitors and batteries: A review, Sustainable Materials and Technologies. 25 (2020) e00190. https://doi.org/10.1016/j.susmat.2020.e00190.

[28] S.H. Park, G. Goodall, W.S. Kim, Perspective on 3D-designed micro-supercapacitors, Materials & Design. 193 (2020) 108797. https://doi.org/10.1016/j.matdes.2020.108797.

[29] S.H.R. Sanei, D. Popescu, 3D-Printed Carbon Fiber Reinforced Polymer Composites: A Systematic Review, J. Compos. Sci. 4 (2020) 98. https://doi.org/10.3390/jcs4030098.

[30] S.F.A. Acquah, B.E. Leonhardt, M.S. Nowotarski, J.M. Magi, K.A. Chambliss, T.E.S. Venzel, S.D. Delekar, L.A. Al-Hariri, Carbon Nanotubes and Graphene as Additives in 3D Printing, in: M.R. Berber, I.H. Hafez (Eds.), Carbon Nanotubes - Current Progress of Their Polymer Composites, InTech, 2016. https://doi.org/10.5772/63419.

[31] H. Guo, R. Lv, S. Bai, Recent advances on 3D printing graphene-based composites, Nano Materials Science. 1 (2019) 101–115. https://doi.org/10.1016/j.nanoms.2019.03.003.

[32] A. Abdalla, H.H. Hamzah, O. Keattch, D. Covill, B.A. Patel, Augmentation of conductive pathways in carbon black/PLA 3D-printed electrodes achieved through varying printing parameters, Electrochimica Acta. 354 (2020) 136618. https://doi.org/10.1016/j.electacta.2020.136618.

[33] H. Steldinger, A. Esposito, K. Brunnengräber, J. Gläsel, B.J.M. Etzold, Activated Carbon in the Third Dimension—3D Printing of a Tuned Porous Carbon, Adv. Sci. 6 (2019) 1901340. https://doi.org/10.1002/advs.201901340.

[34] X. Zhou, C. Liu, Three-dimensional printing of porous carbon structures with tailorable pore sizes, Catalysis Today. 347 (2018) 2–9. https://doi.org/10.1016/j.cattod.2018.05.044.

[35] A. Szczurek, A. Ortona, L. Ferrari, E. Rezaei, G. Medjahdi, V. Fierro, D. Bychanok, P. Kuzhir, A. Celzard, Carbon periodic cellular architectures, Carbon. 88 (2015) 70–85. https://doi.org/10.1016/j.carbon.2015.02.069.

[36] J. Luo, Y. Yao, M. Niu, X. Duan, R. Wang, T. Liu, Direct Laser Writing-Assisted Method for Template-Free Fabrication of Biomass-Based Porous Carbon Platelets with Uniform Size and Arbitrarily Designed Shapes, ACS Omega. 4 (2019) 5870–5878. https://doi.org/10.1021/acsomega.9b00408.

[37] J. Sha, Y. Li, R. Villegas Salvatierra, T. Wang, P. Dong, Y. Ji, S.-K. Lee, C. Zhang, J. Zhang, R.H. Smith, P.M. Ajayan, J. Lou, N. Zhao, J.M. Tour, Three-Dimensional Printed Graphene Foams, ACS Nano. 11 (2017) 6860–6867. https://doi.org/10.1021/acsnano.7b01987.

[38] A. Mazzoli, Selective laser sintering in biomedical engineering, Med Biol Eng Comput. 51 (2013) 245–256. https://doi.org/10.1007/s11517-012-1001-x.

[39] S. Vyavahare, S. Teraiya, D. Panghal, S. Kumar, Fused deposition modelling: a review, RPJ. 26 (2020) 176–201. https://doi.org/10.1108/RPJ-04-2019-0106.

[40] V.G. Rocha, E. Saiz, I.S. Tirichenko, E. García-Tuñón, Direct ink writing advances in multi-material structures for a sustainable future, J. Mater. Chem. A. 8 (2020) 15646–15657. https://doi.org/10.1039/D0TA04181E.

[41] Y. Guo, H.S. Patanwala, B. Bognet, A.W.K. Ma, Inkjet and inkjet-based 3D printing: connecting fluid properties and printing performance, Rapid Prototyping Journal. 23 (2017) 562–576. https://doi.org/10.1108/RPJ-05-2016-0076.

[42] N.J. Wilkinson, M.A.A. Smith, R.W. Kay, R.A. Harris, A review of aerosol jet printing—a non-traditional hybrid process for micro-manufacturing, Int J Adv Manuf Technol. 105 (2019) 4599–4619. https://doi.org/10.1007/s00170-019-03438-2.

[43] S. Mirzababaei, S. Pasebani, A Review on Binder Jet Additive Manufacturing of 316L Stainless Steel, JMMP. 3 (2019) 82. https://doi.org/10.3390/jmmp3030082.

[44] J.Z. Manapat, Q. Chen, P. Ye, R.C. Advincula, 3D Printing of Polymer Nanocomposites via Stereolithography, Macromol. Mater. Eng. 302 (2017) 1600553. https://doi.org/10.1002/mame.201600553.

[45] B. Zhang, S. Li, H. Hingorani, A. Serjouei, L. Larush, A.A. Pawar, W.H. Goh, A.H. Sakhaei, M. Hashimoto, K. Kowsari, S. Magdassi, Q. Ge, Highly stretchable hydrogels for UV curing based high-resolution multimaterial 3D printing, J. Mater. Chem. B. 6 (2018) 3246–3253. https://doi.org/10.1039/C8TB00673C.

[46] J. Zhang, Q. Hu, S. Wang, J. Tao, M. Gou, Digital Light Processing Based Three-dimensional Printing for Medical Applications, International Journal of Bioprinting. 6 (2020). https://doi.org/10.18063/ijb.v6i1.242.

[47] H.O.T. Ware, A.C. Farsheed, E. Baker, G. Ameer, C. Sun, Fabrication Speed Optimization for High-resolution 3D-printing of Bioresorbable Vascular Scaffolds, Procedia CIRP. 65 (2017) 131–138. https://doi.org/10.1016/j.procir.2017.04.038.

[48] X. Zhou, Y. Hou, J. Lin, A review on the processing accuracy of two-photon polymerization, AIP Advances. 5 (2015) 030701. https://doi.org/10.1063/1.4916886.

[49] A. Selimis, V. Mironov, M. Farsari, Direct laser writing: Principles and materials for scaffold 3D printing, Microelectronic Engineering. 132 (2015) 83–89. https://doi.org/10.1016/j.mee.2014.10.001.

[50] B.E. Kelly, I. Bhattacharya, H. Heidari, M. Shusteff, C.M. Spadaccini, H.K. Taylor, Volumetric additive manufacturing via tomographic reconstruction, Science. 363 (2019) 1075–1079. https://doi.org/10.1126/science.aau7114.

[51] I. Gibson, D. Rosen, B. Stucker, Directed Energy Deposition Processes, in: Additive Manufacturing Technologies, Springer New York, New York, NY, 2015: pp. 245–268. https://doi.org/10.1007/978-1-4939-2113-3_10.

[52] R. Sharma, N.L. Ravikumar, K. Dasgupta, J.K. Chakravartty, K.K. Kar, Advanced Carbon–Carbon Composites: Processing Properties and Applications, in: K.K. Kar (Ed.), Composite Materials, Springer Berlin Heidelberg, Berlin, Heidelberg, 2017: pp. 315–367. https://doi.org/10.1007/978-3-662-49514-8_10.

[53] A. Jansson, L. Pejryd, Characterisation of carbon fibre-reinforced polyamide manufactured by selective laser sintering, Additive Manufacturing. 9 (2015) 7–13. https://doi.org/10.1016/j.addma.2015.12.003.

[54] B. Chen, S. Berretta, R. Davies, O. Ghita, Characterisation of carbon fibre (Cf) - Poly Ether Ketone (PEK) composite powders for laser sintering, Polymer Testing. 76 (2019) 65–72. https://doi.org/10.1016/j.polymertesting.2019.03.011.

[55] X. Tian, T. Liu, C. Yang, Q. Wang, D. Li, Interface and performance of 3D printed continuous carbon fiber reinforced PLA composites, Composites Part A: Applied Science and Manufacturing. 88 (2016) 198–205. https://doi.org/10.1016/j.compositesa.2016.05.032.

[56] M. Heidari-Rarani, M. Rafiee-Afarani, A.M. Zahedi, Mechanical characterization of FDM 3D printing of continuous carbon fiber reinforced PLA composites, Composites Part B: Engineering. 175 (2019) 107147. https://doi.org/10.1016/j.compositesb.2019.107147.

[57] M.N. Jahangir, K.M.M. Billah, Y. Lin, D.A. Roberson, R.B. Wicker, D. Espalin, Reinforcement of material extrusion 3D printed polycarbonate using continuous carbon fiber, Additive Manufacturing. 28 (2019) 354–364. https://doi.org/10.1016/j.addma.2019.05.019.

[58] W. Ye, G. Lin, W. Wu, P. Geng, X. Hu, Z. Gao, J. Zhao, Separated 3D printing of continuous carbon fiber reinforced thermoplastic polyimide, Composites Part A: Applied Science and Manufacturing. 121 (2019) 457–464. https://doi.org/10.1016/j.compositesa.2019.04.002.

[59] Y. Peng, Y. Wu, K. Wang, G. Gao, S. Ahzi, Synergistic reinforcement of polyamide-based composites by combination of short and continuous carbon fibers via fused filament fabrication, Composite Structures. 207 (2019) 232–239. https://doi.org/10.1016/j.compstruct.2018.09.014.

[60] Y. Peng, Y. Wu, S. Li, K. Wang, S. Yao, Z. Liu, H. Garmestani, Tailorable rigidity and energy-absorption capability of 3D printed continuous carbon fiber reinforced polyamide composites, Composites Science and Technology. 199 (2020) 108337. https://doi.org/10.1016/j.compscitech.2020.108337.

[61] P. Parandoush, C. Zhou, D. Lin, 3D Printing of Ultrahigh Strength Continuous Carbon Fiber Composites, Adv. Eng. Mater. 21 (2019) 1800622. https://doi.org/10.1002/adem.201800622.

[62] B. Chang, X. Li, P. Parandoush, S. Ruan, C. Shen, D. Lin, Additive manufacturing of continuous carbon fiber reinforced poly-ether-ether-ketone with ultrahigh mechanical properties, Polymer Testing. 88 (2020) 106563. https://doi.org/10.1016/j.polymertesting.2020.106563.

[63] H. Guo, M.B. Gingerich, L.M. Headings, R. Hahnlen, M.J. Dapino, Joining of carbon fiber and aluminum using ultrasonic additive manufacturing (UAM), Composite Structures. 208 (2018) 180–188. https://doi.org/10.1016/j.compstruct.2018.10.004.

[64] X. Yi, Z.-J. Tan, W.-J. Yu, J. Li, B.-J. Li, B.-Y. Huang, J. Liao, Three dimensional printing of carbon/carbon composites by selective laser sintering, Carbon. 96 (2015) 603–607. https://doi.org/10.1016/j.carbon.2015.09.110.

[65] P. Wang, B. Zhang, C.C. Tan, S. Raghavan, Y.-F. Lim, C.-N. Sun, J. Wei, D. Chi, Microstructural characteristics and mechanical properties of carbon nanotube reinforced Inconel 625 parts fabricated by selective laser melting, Materials & Design. 112 (2016) 290–299. https://doi.org/10.1016/j.matdes.2016.09.080.

[66] Y. Kutlu, Y.L. Wencke, G.A. Luinstra, C. Esen, A. Ostendorf, Directed Energy Deposition of PA12 carbon nanotube composite powder using a fiber laser, in: 2020. https://doi.org/10.1016/j.procir.2020.09.025.

[67] I.A. Kinloch, J. Suhr, J. Lou, R.J. Young, P.M. Ajayan, Composites with carbon nanotubes and graphene: An outlook, Science. 362 (2018) 547–553. https://doi.org/10.1126/science.aat7439.

[68] H.K. Sezer, O. Eren, FDM 3D printing of MWCNT re-inforced ABS nano-composite parts with enhanced mechanical and electrical properties, Journal of Manufacturing Processes. 37 (2019) 339–347. https://doi.org/10.1016/j.jmapro.2018.12.004.

[69] B. Chang, X. Li, P. Parandoush, S. Ruan, C. Shen, D. Lin, Additive manufacturing of continuous carbon fiber reinforced poly-ether-ether-ketone with ultrahigh mechanical properties, Polymer Testing. 88 (2020) 106563. https://doi.org/10.1016/j.polymertesting.2020.106563.

[70] R. Hong, Z. Zhao, J. Leng, J. Wu, J. Zhang, Two-step approach based on selective laser sintering for high performance carbon black/ polyamide 12 composite with 3D segregated conductive network, Composites Part B: Engineering. 176 (2019) 107214. https://doi.org/10.1016/j.compositesb.2019.107214.

[71] U.S. Jayapiriya, S. Goel, Surface modified 3D printed carbon bioelectrodes for glucose/O2 enzymatic biofuel cell: Comparison and optimization, Sustainable Energy Technologies and Assessments. 42 (2020) 100811. https://doi.org/10.1016/j.seta.2020.100811.

[72] M.P. Browne, F. Novotný, Z. Sofer, M. Pumera, 3D Printed Graphene Electrodes' Electrochemical Activation, ACS Appl. Mater. Interfaces. 10 (2018) 40294–40301. https://doi.org/10.1021/acsami.8b14701.

[73] R. Gusmão, M.P. Browne, Z. Sofer, M. Pumera, The capacitance and electron transfer of 3D-printed graphene electrodes are dramatically influenced by the type of solvent used for pre-treatment, Electrochemistry Communications. 102 (2019) 83–88. https://doi.org/10.1016/j.elecom.2019.04.004.

[74] A.C. de Leon, B.J. Rodier, C. Bajamundi, A. Espera, P. Wei, J.G. Kwon, J. Williams, F. Ilijasic, R.C. Advincula, E. Pentzer, Plastic Metal-Free Electric Motor by 3D

Printing of Graphene-Polyamide Powder, ACS Appl. Energy Mater. 1 (2018) 1726–1733. https://doi.org/10.1021/acsaem.8b00240.

[75] B. Luo, Y. Wei, H. Chen, Z. Zhu, P. Fan, X. Xu, B. Xie, Printing Carbon Nanotube-Embedded Silicone Elastomers via Direct Writing, ACS Appl. Mater. Interfaces. 10 (2018) 44796–44802. https://doi.org/10.1021/acsami.8b18614.

[76] Q. Li, S. Luo, Y. Wang, Q.-M. Wang, Carbon based polyimide nanocomposites thin film strain sensors fabricated by ink-jet printing method, Sensors and Actuators A: Physical. 300 (2019) 111664. https://doi.org/10.1016/j.sna.2019.111664.

[77] U. Staudinger, G. Zyla, B. Krause, A. Janke, D. Fischer, C. Esen, B. Voit, A. Ostendorf, Development of electrically conductive microstructures based on polymer/CNT nanocomposites via two-photon polymerization, Microelectronic Engineering. 179 (2017) 48–55. https://doi.org/10.1016/j.mee.2017.04.024.

[78] Y. Liu, W. Xiong, L.J. Jiang, Y. Zhou, D. Li, L. Jiang, J.-F. Silvain, Y. Lu, Laser-directed 3D assembly of carbon nanotube using Two-photon polymerization, in: 2017. https://doi.org/10.1117/12.2257051.

[79] Y. Zuo, Z. Yao, H. Lin, J. Zhou, J. Lu, J. Ding, Digital light processing 3D printing of graphene/carbonyl iron/polymethyl methacrylate nanocomposites for efficient microwave absorption, Composites Part B: Engineering. 179 (2019) 107533. https://doi.org/10.1016/j.compositesb.2019.107533.

[80] H. Cui, Y. Yu, X. Li, Z. Sun, J. Ruan, Z. Wu, J. Qian, J. Yin, Direct 3D printing of a tough hydrogel incorporated with carbon nanotubes for bone regeneration, J. Mater. Chem. B. 7 (2019) 7207–7217. https://doi.org/10.1039/C9TB01494B.

[81] A. Celzard, V. Fierro, “Green”, innovative, versatile and efficient carbon materials from polyphenolic plant extracts, Carbon. 167 (2020) 792–815. https://doi.org/10.1016/j.carbon.2020.05.053.

[82] Q. Zhang, F. Zhang, S.P. Medarametla, H. Li, C. Zhou, D. Lin, 3D Printing of Graphene Aerogels, Small. 12 (2016) 1702–1708. https://doi.org/10.1002/smll.201503524.

[83] M. Peng, Z. Wen, L. Xie, J. Cheng, Z. Jia, D. Shi, H. Zeng, B. Zhao, Z. Liang, T. Li, L. Jiang, 3D Printing of Ultralight Biomimetic Hierarchical Graphene Materials with Exceptional Stiffness and Resilience, Adv. Mater. 31 (2019) 1902930. https://doi.org/10.1002/adma.201902930.

[84] P. Kuzhir, A. Paddubskaya, D. Bychanok, A. Liubimau, A. Ortona, V. Fierro, A. Celzard, 3D-printed, carbon-based, lossy photonic crystals: Is high electrical conductivity the must?, Carbon. 171 (2020) 484–492. https://doi.org/10.1016/j.carbon.2020.09.020.

[85] X. Chen, G. Zhao, Y. Wu, Y. Huang, Y. Liu, J. He, L. Wang, Q. Lian, D. Li, Cellular carbon microstructures developed by using stereolithography, Carbon. 123 (2017) 34–44. https://doi.org/10.1016/j.carbon.2017.07.043.

[86] Y. Ge, T. Zhang, B. Zhou, H. Wang, Z. Zhang, J. Shen, A. Du, Nanostructured resorcinol-formaldehyde ink for 3D direct writing, J. Mater. Res. 33 (2018) 2052–2061. https://doi.org/10.1557/jmr.2018.104.

[87] B. Bian, D. Shi, X. Cai, M. Hu, Q. Guo, C. Zhang, Q. Wang, A.X. Sun, J. Yang, 3D printed porous carbon anode for enhanced power generation in microbial fuel cell, Nano Energy. 44 (2018) 174–180. https://doi.org/10.1016/j.nanoen.2017.11.070.

[88] B. Rezaei, J.Y. Pan, C. Gundlach, S.S. Keller, Highly structured 3D pyrolytic carbon electrodes derived from additive manufacturing technology, Materials & Design. 193 (2020) 108834. https://doi.org/10.1016/j.matdes.2020.108834.

[89] P. Wang, H. Zhang, H. Wang, D. Li, J. Xuan, L. Zhang, Hybrid Manufacturing of 3D Hierarchical Porous Carbons for Electrochemical Storage, Adv. Mater. Technol. 5 (2020) 1901030. https://doi.org/10.1002/admt.201901030.

[90] S. Kwon, G. Kim, H. Lim, J. Kim, K.-B. Choi, J. Lee, High performance microsupercapacitors based on a nano-micro hierarchical carbon electrode by direct laser writing, Appl. Phys. Lett. 113 (2018) 243901. https://doi.org/10.1063/1.5066017.

[91] C. Yang, Q. Cao, P. Puthongkham, S.T. Lee, M. Ganesana, N.V. Lavrik, B.J. Venton, 3D-Printed Carbon Electrodes for Neurotransmitter Detection, Angew. Chem. Int. Ed. 57 (2018) 14255–14259. https://doi.org/10.1002/anie.201809992.

[92] Q. Cao, M. Shin, N.V. Lavrik, B.J. Venton, 3D-Printed Carbon Nanoelectrodes for In Vivo Neurotransmitter Sensing, Nano Lett. 20 (2020) 6831–6836. https://doi.org/10.1021/acs.nanolett.0c02844.

[93] Y. Shao, C. Guizani, P. Grosseau, D. Chaussy, D. Beneventi, Use of lignocellulosic materials and 3D printing for the development of structured monolithic carbon materials, Composites Part B: Engineering. 149 (2018) 206–215. https://doi.org/10.1016/j.compositesb.2018.05.035.

[94] J. Roman, W. Neri, V. Fierro, A. Celzard, A. Bentaleb, I. Ly, J. Zhong, A. Derré, P. Poulin, Lignin-graphene oxide inks for 3D printing of graphitic materials with tunable density, Nano Today. 33 (2020) 100881. https://doi.org/10.1016/j.nantod.2020.100881.

[95] J.P. Llinas, M.A. Hekmaty, A.A. Talin, F. Léonard, Origami Terahertz Detectors Realized by Inkjet Printing of Carbon Nanotube Inks, ACS Appl. Nano Mater. 3 (2020) 2920–2927. https://doi.org/10.1021/acsanm.0c00182.

[96] B. Chen, Y. Jiang, X. Tang, Y. Pan, S. Hu, Fully Packaged Carbon Nanotube Supercapacitors by Direct Ink Writing on Flexible Substrates, ACS Appl. Mater. Interfaces. 9 (2017) 28433–28440. https://doi.org/10.1021/acsami.7b06804.

[97] W. Yu, H. Zhou, B.Q. Li, S. Ding, 3D Printing of Carbon Nanotubes-Based Microsupercapacitors, ACS Appl. Mater. Interfaces. 9 (2017) 4597–4604. https://doi.org/10.1021/acsami.6b13904.

[98] Y. Jiang, Z. Xu, T. Huang, Y. Liu, F. Guo, J. Xi, W. Gao, C. Gao, Direct 3D Printing of Ultralight Graphene Oxide Aerogel Microlattices, Adv. Funct. Mater. 28 (2018) 1707024. https://doi.org/10.1002/adfm.201707024.

[99] M. Idrees, S. Ahmed, Z. Mohammed, N.S. Korivi, V. Rangari, 3D printed supercapacitor using porous carbon derived from packaging waste, Additive Manufacturing. 36 (2020) 101525. https://doi.org/10.1016/j.addma.2020.101525.

[100] S.D. Lacey, D.J. Kirsch, Y. Li, J.T. Morgenstern, B.C. Zarket, Y. Yao, J. Dai, L.Q. Garcia, B. Liu, T. Gao, S. Xu, S.R. Raghavan, J.W. Connell, Y. Lin, L. Hu, Extrusion-Based 3D Printing of Hierarchically Porous Advanced Battery Electrodes, Adv. Mater. 30 (2018) 1705651. https://doi.org/10.1002/adma.201705651.

[101] Y. Qiao, Y. Liu, C. Chen, H. Xie, Y. Yao, S. He, W. Ping, B. Liu, L. Hu, 3D-Printed Graphene Oxide Framework with Thermal Shock Synthesized Nanoparticles for Li-CO_2 Batteries, Adv. Funct. Mater. 28 (2018) 1805899. https://doi.org/10.1002/adfm.201805899.

[102] G.L. Goh, S. Agarwala, W.Y. Yeong, Aerosol-Jet-Printed Preferentially Aligned Carbon Nanotube Twin-Lines for Printed Electronics, ACS Appl. Mater. Interfaces. 11 (2019) 43719–43730. https://doi.org/10.1021/acsami.9b15060.

[103] S. Lu, J. Zheng, J.A. Cardenas, N.X. Williams, Y.-C. Lin, A.D. Franklin, Uniform and Stable Aerosol Jet Printing of Carbon Nanotube Thin-Film Transistors by Ink Temperature Control, ACS Appl. Mater. Interfaces. 12 (2020) 43083–43089. https://doi.org/10.1021/acsami.0c12046.

[104] K. Parate, S.V. Rangnekar, D. Jing, D.L. Mendivelso-Perez, S. Ding, E.B. Secor, E.A. Smith, J.M. Hostetter, M.C. Hersam, J.C. Claussen, Aerosol-Jet-Printed Graphene Immunosensor for Label-Free Cytokine Monitoring in Serum, ACS Appl. Mater. Interfaces. 12 (2020) 8592–8603. https://doi.org/10.1021/acsami.9b22183.